Montanuniversität Leoben
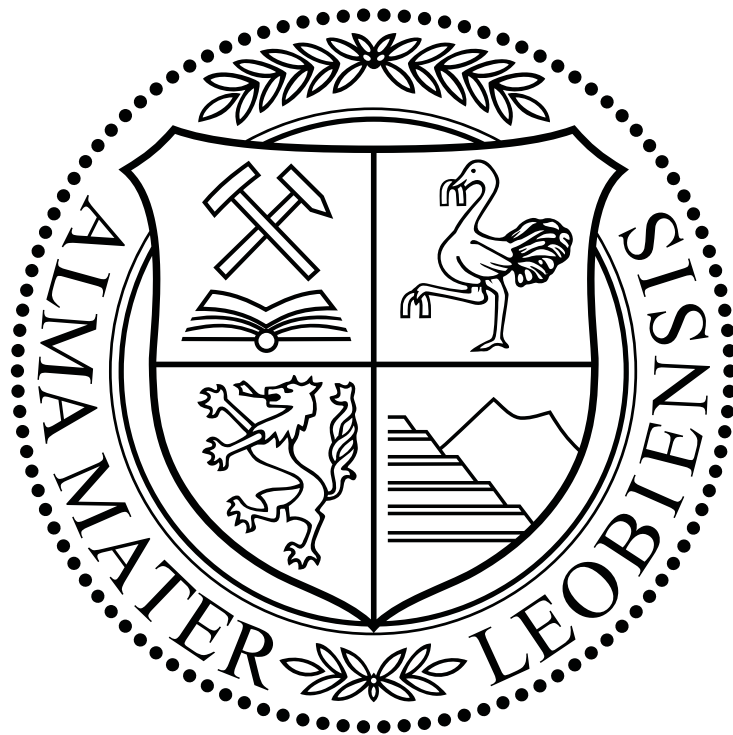
Additive Manufacturing of a β-Solidifying γ-Titanium Aluminide Alloy

Richard Bürstmayr

May 2018

The following work was conducted at the Department of Physical Metallurgy and Materials Testing, Montanuniversität Leoben. The sample material was provided by Neue Materialien Fürth GmbH, Fürth, Germany.

Affidavit

I declare in lieu of oath that I wrote this thesis and performed the associated research myself, using only literature cited in this volume.

May 2018, Leoben   Richard Bürstmayr

Acknowledgements

I would like to thank Univ.-Prof. DI Dr.mont. Helmut Clemens and Ass.Prof. DI Dr.mont. Svea Mayer for the opportunity to conduct this master thesis and continuous support during the months of work.

My sincere gratitude goes to my colleagues at the Department of Physical Metallurgy and Materials Testing for the positive work environment as well as providing helpful insights and interesting discussions. In particular the doctoral students of the TiAl-group and Gerhard Hawranek are worthy of mention in this context.

For their input I thank Dr. Martin Franke, Dr. Martin Schloffer and Dr. Michael Kastenhuber who contributed to the success of this thesis.

My biggest thanks go to my family, my parents Maria and Hermann for supporting me throughout my studies as well as all other circumstances of life as well as my brothers Eduard and Georg.

Thank you all!

Contents

Abbreviations and symbols

α   α-Ti(Al), a disordered hexagonal close packed solid solution

$α_2$ $α_2$-Ti$_3$Al, an ordered intermetallic phase with DO$_{19}$ structure

β   β-Ti(Al), a disordered body centered cubic solid solution

$β_o$ $β_o$-TiAl, an ordered intermetallic phase with B2 structure

γ   γ-TiAl, an odered intermetallic phase with L1$_0$ structure

ε   creep strain

$\dot{ε}$ creep strain rate

θ   diffraction angle

λ   wavelength

ν   electron beam scanning speed

φ   logarithmic degree of deformation (true strain)

$\dot{φ}$ logarithmic strain rate

AC   air cooling

AM   additive manufacturing

at.%   atomic percent

bcc   body centered cubic

BDTT   brittle-to-ductile transition temperature

BSE   back-scattered electrons

CNC   computerized numerical control

DSC   differential scanning calorimetry

EBM   electron beam melting

EBSD   electron back-scatter diffraction

EDX   energy dispersive X-ray spectroscopy

FC   furnace cooling

FL   fully lamellar

hcp	hexagonal close-packed
HIP	hot isostatic pressing
I	current
k_f	true stress (flow stress)
$k_{f,max}$	maximal flow stress
L	liquid
LE	line energy
LEAP	leading edge aviation propulsion
LOM	light optical microscope
m.%	mass percent
NL	nearly lamellar
OPS	oxide polishing suspension
R_m	tensile strength
$R_{p0.1}$	0.1% offset yield strength
$R_{p0.2}$	0.2% offset yield strength
RT	room temperature
SE	secondary electrons
SEBM	selective electron beam melting
SEM	scanning electron microscope
SM	subtractive manufacturing
t	time
T_β	β-transus temperature
$T_{\gamma\text{-solv}}$	γ-solvus temperature
T_{eut}	eutectoid temperature
T_{liq}	liquidus temperature
T_{sol}	solidus temperature
Ti-6Al-4V	a Ti-alloy with a nominal composition of Ti, 6 m.% Al and 4 m.% V
TiAl	titanium aluminide

TNM   a β-solidifying γ-TiAl based alloy containing Nb and Mo

U   acceleration voltage

VIGA   vaccuum induction melting inert gas atomization

VIM   vacuum induction melting

vol.%   volume percent

XRD   X-ray diffraction

1   Introduction

Additive manufacturing (AM) methods use computer based models to produce geometrically complicated three-dimensional products. In contrast to so-called subtractive manufacturing (SM) methods, such as computerized numerical controlled (CNC) milling, which rely on the removal of material to create complex parts, in AM material is added locally in order to create a near net shape product. Ideally this leads to a higher utilization of material and production speed while decreasing the need for later machining, thus increasing overall productivity [1]. One of the major challenges is to find suitable manufacturing methods to gain ideal material properties while still being able to produce in a fast and cheap way. The range of materials to which AM methods are applicable has grown steadily since the 1980s when for the first time polymers were 3D printed [2] and now includes metals, ceramics and others [1, 3, 4]. One approach to AM are powder bed fusion methods where a precursor powder is introduced layer by layer into a build chamber and then molten or sintered by an external energy source. This enables the production of very complex structures that can even contain internal features, which are very difficult to achieve by SM methods, while minimizing the necessity for machining. Another advantage of these methods is the chance to recycle the unused powder to be used again in further parts leading to a high material yield [1, 5].

For (inter-)metallic materials electron beam melting (EBM or selective electron beam melting, SEBM) is a versatile powder bed fusion method to produce high quality near net shape parts. Since its introduction into the market by Arcam (Sweden) in the late 1990s, this technology has been successfully employed in a variety of metallic materials, for example the most common α-β-Ti alloy Ti-6Al-4V (in m.%), steels as well as Ni- and Co- based alloys [1]. In 2017 for the first time a 3D-printed nozzle from a Ni-alloy has been introduced inside the LEAP jet engine by GE and the first LEAP powered Airbus A320neo started ferrying paying passengers in the summer of 2017 [6, 7].

In order to improve the efficiency and performance of engines in the automotive and aerospace industry higher turning rates of turbines and increased combustion gas temperatures are necessary. This means that the materials need to satisfy these increasingly challenging requirements with regard to density, creep resistance and high-temperature strength. One class of materials that arose from this set of "circumstances" are the intermetallic γ-titanium aluminides (TiAl) which show promising material properties with regards to application at high temperatures. These include good creep properties, high strength and good oxidation resistance in a temper-

ature range of up to 800 °C. All of these qualities are combined with a low density in comparison to other commonly used high temperature materials, such as Ni-base alloys. As a consequence they have seen increased use in recent years, especially in the aerospace sector [8, 9]. An additive manufacturing factory in Cameri, Italy, is already printing TiAl turbine blades [7].

This work aims to investigate the properties of a powder metallurgical TiAl alloy known as TNM (acronym for Titanium-Aluminide-Niobium-Molybdenum), fabricated by means of EBM. To that end several cylindrical test specimens have been manufactured in an EBM-machine with powder produced by vacuum induction melting inert gas atomization (VIGA) for later investigation on their microstructure, strength and creep properties.

2 Fundamentals

2.1 Alloy System

2.1.1 The Ti-Al-System

The basis of the TNM alloy is the binary system Ti-Al. It therefore helps to first consider this phase diagram in order to better understand the alloy. A thorough investigation of this system has been conducted by Schuster and Palm [10], which resulted in the phase diagram displayed in figure 2.1.
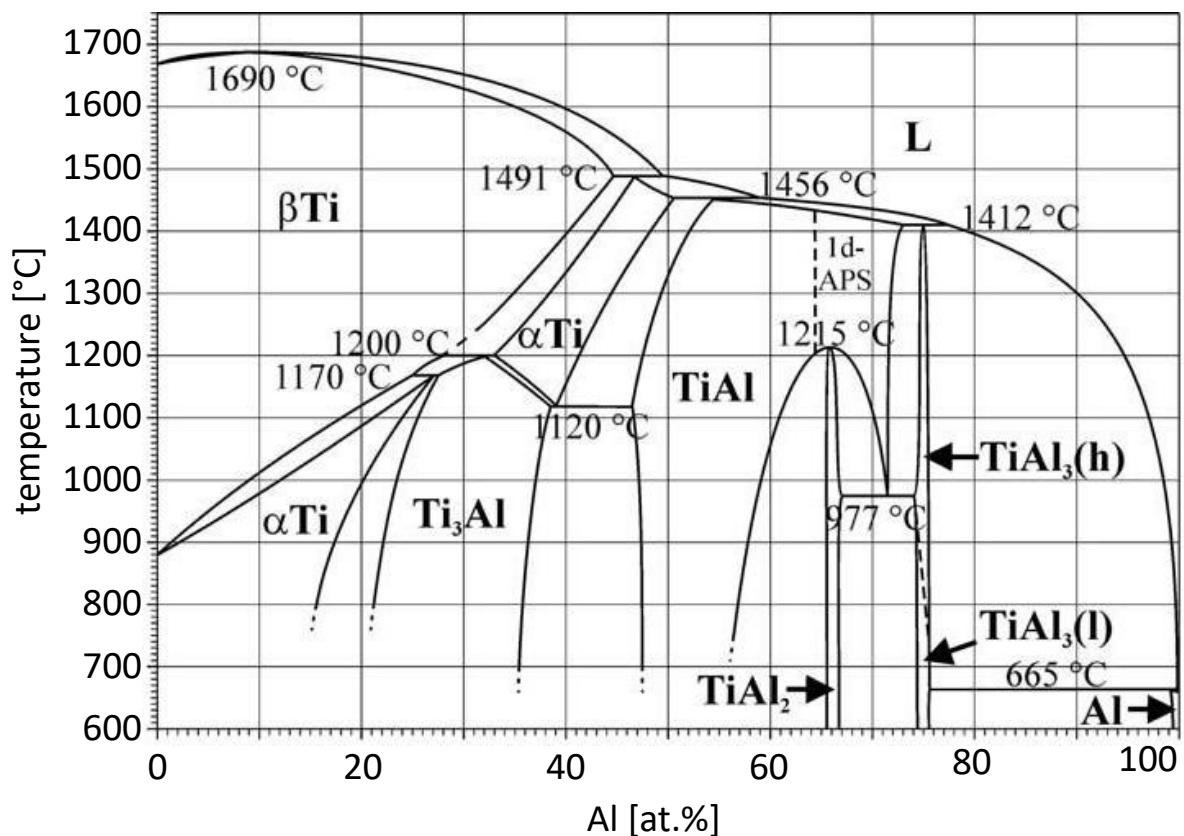
Figure 2.1: The binary Ti-Al phase diagram as published by Schuster and Palm [10]. The relevant part of the phase diagram for γ-TiAl alloys ranges between around 40 and 50 at.% Al.

The interesting concentration range for γ-TiAl alloys lies between roughly 40 and 50 at.% Al. For lower Al-concentrations within this concentration range the binary system solidifies via the β-phase. At lower temperatures the α- and γ-phases precipitate, for further details see section 2.1.5. Above the β-transus temperature ($T_β$) only the β-phase is thermodynamically stable,

below the γ-solvus temperature ($T_{\gamma\text{-solv}}$) the γ-phase coexists. For increased Al-concentrations the solidification takes place through a peritectic reaction. In this case the α-phase is stable at higher temperatures and for Al-concentrations above the peritectic point no β-phase exists after the peritectic reaction L+β→α. With decreasing temperature the γ-phase precipitates [10, 11]. The γ- and α_2-phases are of great importance with regard to the mechanical and creep properties of any γ-TiAl based alloy, a further description is provided in section 2.1.5. By using an appropriate Al-concentration, alloying elements and heat treatments the material properties can be adjusted to optimally suit the respective application conditions, i.e. suitable for use at elevated temperatures and under higher mechanical loading [8, 11, 12].

2.1.2 Phases and Crystalline Structures

For high temperatures the prevalent phase below 45 at.% Al is the disordered body centered cubic (bcc, A2 structure, Im$\overline{3}$m) β-phase. At lower temperatures an ordering transition occurs and the β-lattice transforms into the bcc B2-ordered (Pm$\overline{3}$m) β_o. This ordered β_o-phase has a detrimental influence on the material properties, in particular on the creep properties [8, 13]. However, due to its high number of independent slip systems, its disordered high temperature counterpart β allows a better deformability at elevated temperatures and thus the forging of the material [13].

The hexagonal close packed (hcp, A3 structure, P6$_3$/mmc) α-phase is stable at lower temperatures or higher Al-concentrations in comparison to β. At lower temperatures it transforms into the ordered phase α_2-Ti$_3$Al (D0$_{19}$ structure, P6$_3$/mmc). The order transitions of β/β_o and α/α_2 occur in the temperature range of 1120-1250 °C [10].

The third occurring phase is the face-centered tetragonal L1$_0$ (P4/mmm) γ-TiAl. It is ordered over the entire temperature range of its existence. This phase is "almost" face-centered, with the ratio of c to a of the unit cell being 1.02. However, an increasing Al-concentration increases the tetragonality of the lattice which has a negative influence on the deformability [14]. All of the phases described are represented in figure 2.2.

2.1.3 Alloying Elements

Aluminium

Aluminium is the main element in the alloy and has the major influence on both the solidification as well as the phase constitution of the material at room temperature (RT). For lower Al contents alloys solidify via the L+β two-phase field, while higher concentrations shift the system towards the peritectic reaction. Aluminium stabilizes the α-phase and shifts $T_{\gamma\text{-solv}}$ as well as T_β towards higher values [11].
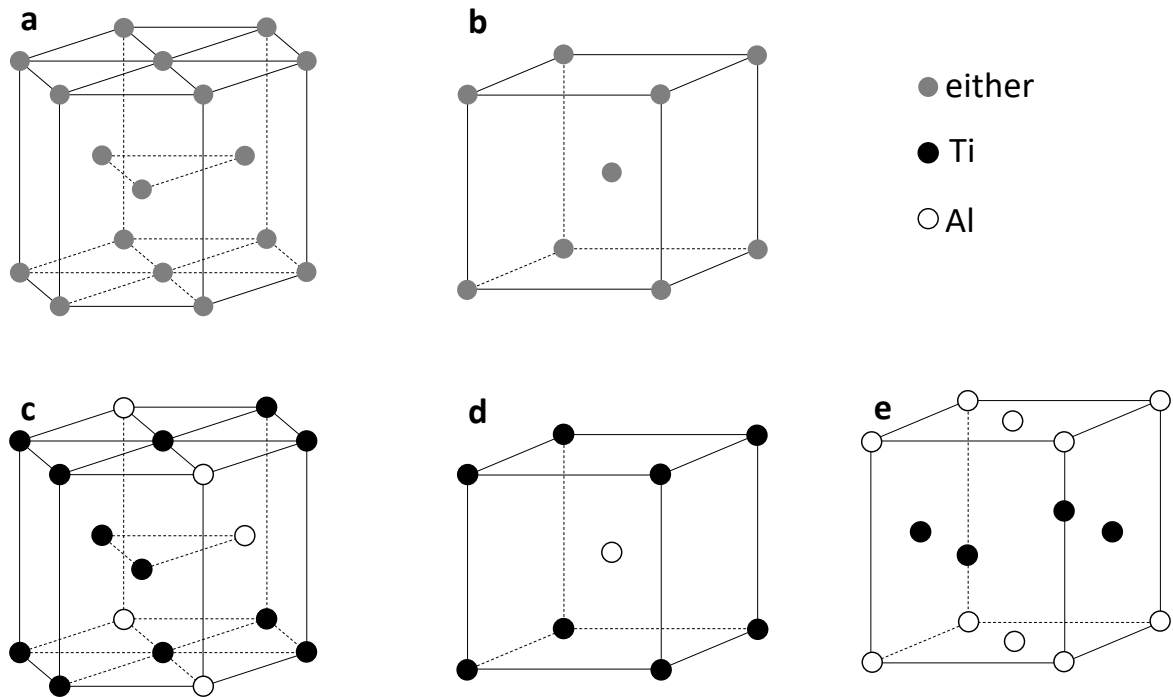
Figure 2.2: The crystal structures of the main phases in the TNM system. **a**: hexagonal A3 (α-Ti(Al)), **b**: bcc A2 (β-Ti(Al)), **c**: hexagonal DO_{19} ($α_2$-Ti_3Al), **d**: bcc B2 ($β_o$-TiAl), **e**: face-centered tetragonal $L1_0$ (γ-TiAl)

Niobium and Molybdenum

The elements Nb and Mo stabilize the β-phase. This is of importance to improve the processing properties at high temperatures, where processes such as extrusion, forging and rolling are carried out and the presence of a sufficient volume fraction of β-phase at hot-working temperature improves the deformability [8, 11]. However, it is also known to reduce high temperature strength and creep resistance in the case of the ordered $β_o$-phase [15]. Despite the fact that Mo is a stronger β-stabilizer than Nb the latter is preferred in terms of oxidation protection as Mo has a negative influence on the oxidation resistance of the material [8]. These elements are also associated with decreasing the diffusion in $α_2$ and γ by increasing the activation energy of diffusion, which in turn improves the creep resistance and high-temperature strength [9]. Both Mo and Nb also tend to segregate strongly during solidification within the cast material [11].

Boron

Boron is mostly used for grain refinement in cast alloys. It aids in the formation of heterogeneous nucleation sites in the form of borides [8, 11]. Whether B affects the behaviour of the TNM when it is produced via EBM is not yet known. Other works on Ti-6Al-4V showed little

influence on the grain size as found by Mahbooba et al. [16].

Other elements

Interstitial elements, such as C and N, have a high solubility in α/α_2. Therefore they stabilize that phase. In particular O has a very high solubility in α of up to 22000 at. ppm [11, 17].

2.1.4 The TNM Phase Diagram

The acronym TNM stands for the alloying elements TiAl - Nb - Mo and describes the β-solidifying γ-TiAl based alloy with the nominal chemical composition of 43.5 at.% Al, 4 at.% Nb, 1 at.% Mo and 0.1 at.% B. This composition is indicated in the quasi-binary phase diagram marked with the red line in figure 2.3 [9].
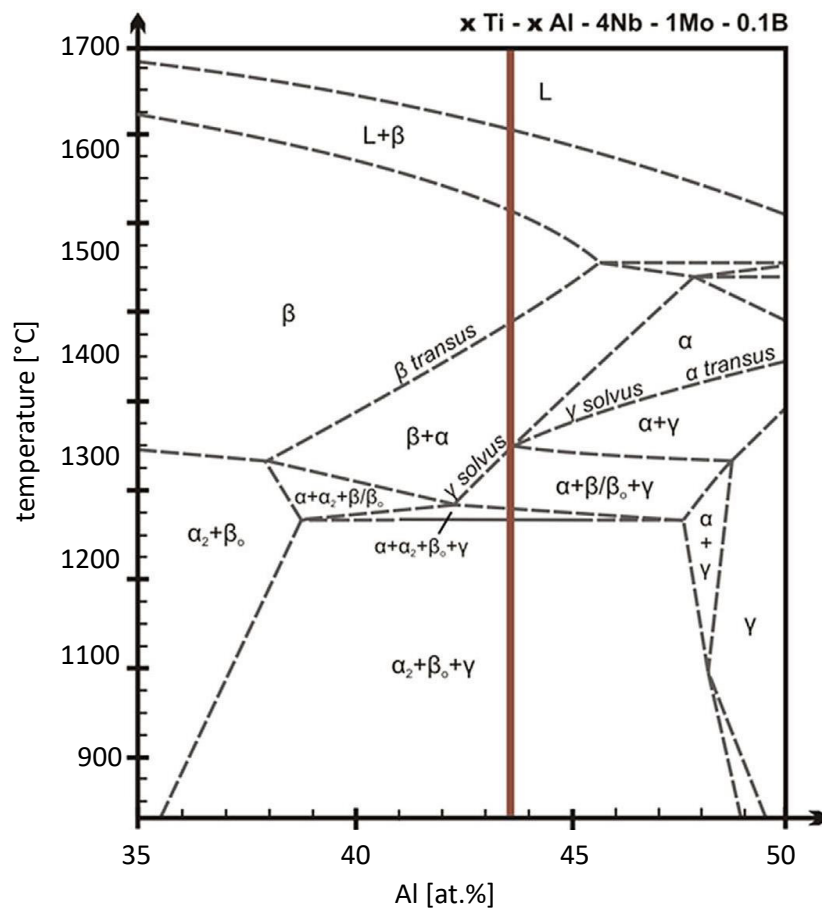
Figure 2.3: Quasi-binary section through the TNM alloying system. The phase diagram is taken from [9]. The vertical line indicates the nominal composition of TNM.

When comparing the phase diagram of TNM with the binary TiAl system the increased area of the $\alpha+\beta$ two-phase field region is apparent. By alloying with the β-stabilizing elements, the size of the β phase field is increased, which is important to improve the hot workability of the alloy.

Since the ordered β_o-phase is brittle and has a detrimental influence on the creep properties of the material, the β_o fraction is kept as low as possible at RT and application temperature by subsequent heat treatments [8].

2.1.5 Phase Transitions and Microstructure

When the material solidifies entirely via the β-phase, shown by the red line in figure 2.3, the phase transformations occur as follows:

$$L \rightarrow L + \beta \rightarrow \beta \rightarrow \alpha + \beta \rightarrow \alpha + \beta + \gamma \rightarrow \alpha + \beta + \beta_o + \gamma$$
$$\rightarrow \alpha + \beta_o + \gamma \rightarrow \alpha + \alpha_2 + \beta_o + \gamma \rightarrow \alpha_2 + \beta_o + \gamma \qquad (2.1)$$
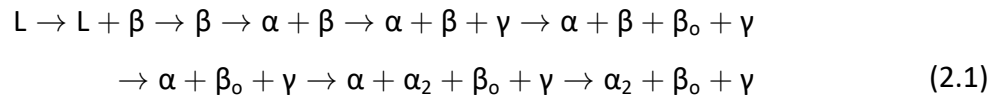
The first solid phase transformation after complete solidification is the precipitation of α from β. This happens according to the Burgers orientation relationship [9, 11]:

$$\{110\}_\beta \| (0001)_\alpha \text{ and } < 111 >_\beta \| < 11\bar{2}0 >_\alpha \qquad (2.2)$$

This results in twelve different ways for α to precipitate from β when considering the six different {110}-planes with two <111>-directions in each of those planes. The precipitation of γ from α_2 is described by the Blackburn orientation relationship [11]:

$$(0001)_{\alpha_2} \| \{111\}_\gamma \text{ and } < 11\bar{2}0 >_{\alpha_2} \| < 1\bar{1}0]_\gamma \qquad (2.3)$$

This means that the (0001)-plane of α determines the orientation of the resulting γ- and α_2-lamellae. Therefore, all the γ-lamellae within a single α_2-domain are oriented parallel to each other [11].

By choosing appropriate heat treatments various microstructures can be achieved in TNM. Annealing in the $\alpha+\beta/\beta_o+\gamma$ phase field followed by a stabilization annealing in the $\alpha_2+\beta_o+\gamma$ phase field leads to a nearly lamellar (NL) microstructure. It is characterized by lamellar $\alpha_2+\gamma$-colonies with globular β_o- and γ-grains at the grain boundaries. For higher Al-contents where an annealing step in the α single phase field is possible a fully lamellar (FL) microstructure can be achieved, where no globular grain boundary phases occur. This microstructure can however not be achieved for the material considered in this work due to its low Al-content. For many high temperature applications one of these microstructures is preferred, as they provide the best creep resistance. However at RT they exhibit poor ductility [8].

When annealing at lower temperatures in the $\alpha+\beta/\beta_o+\gamma$ phase field a duplex or near γ microstructure is formed. A duplex microstructure shows fewer lamellar areas, while in a near

γ structure no more lamellae are visible at all, which exhibits worse creep behaviour than their lamellar counterparts, however the ductility at RT is improved [8, 11, 18].

2.2 Electron Beam Melting

EBM is an additive powder bed fusion process used to manufacture geometrically complex metallic parts. A pre-alloyed atomized precursor powder serves as the base material and an electron beam as the energy source. The system works similar to many electron beam welding machines; a schematic sketch of an EBM apparatus is provided in figure 2.4. An electron gun operating at a current (I) between a range of a mA to A with an acceleration voltage (U) of around 60 kV is used as energy source [1, 19].
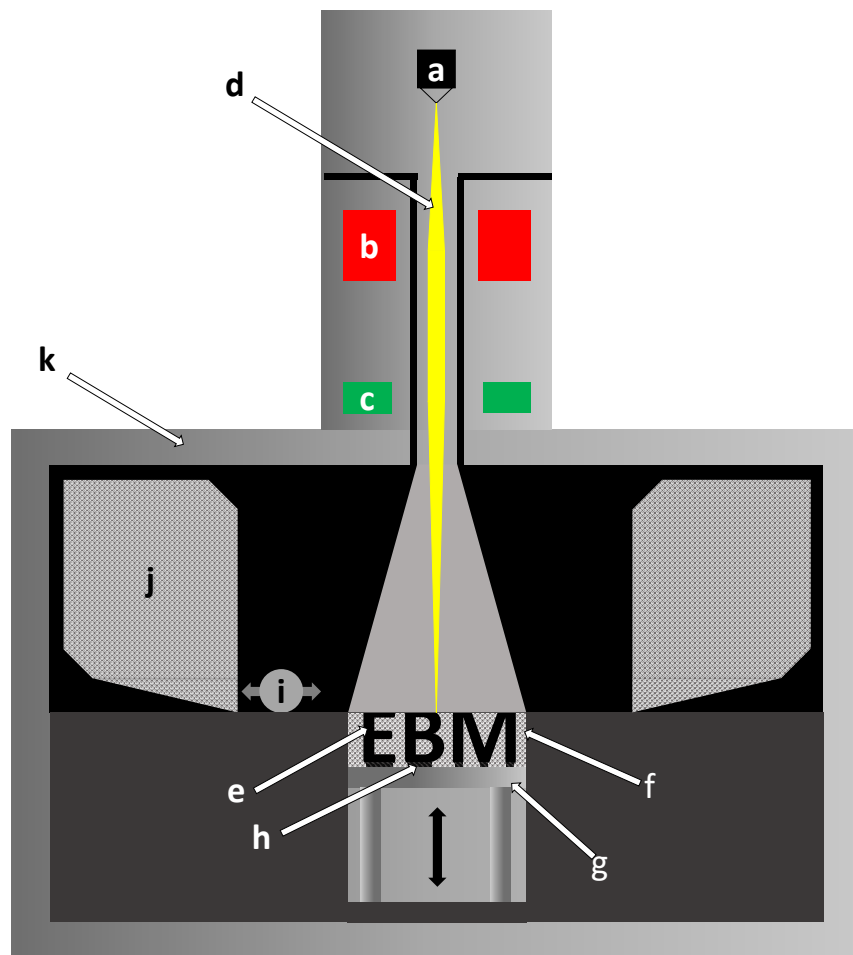
Figure 2.4: Schematic setup of an EBM machine [20]. Description: **a** electron gun, **b** lensing system, **c** deflector lense, **d** electron beam, **e** part under construction, **f** superfluous powder, **g** base plate, **h** support structures, **i** raking system, **j** powder containers, **k** vacuum chamber.

The steps of the process can be described as follows:

1. A three-dimensional computer-aided design (CAD) model of the component to be manufactured is created. This model is subsequently decomposed into two-dimensional sections;

1. The bed is lowered by a defined increment (usually several 10-100 µm);

2. New material is introduced from the powder reservoir on top of the old layer using the raking system (see figure 2.4);

3. One or more heating passes are executed to preheat the material;

4. A final melting pass is used to selectively melt the material based on the data of the respective two-dimensional section. Mostly this is done by melting the contours first and then completing the remaining layer by filling out the rest of the area.

5. Repeat from step 1 [1].

The process begins on a base plate which is usually made of steel. Generally the building material has properties that are different from those of the base plate. Especially differences in the thermal expansion influence the process. The stresses resulting from this difference prevent a construction of the parts directly on the base plate. Another problem is the difference in the chemical composition of the base plate and the building material. To alleviate these problems, a porous support structure is built on the base plate. Upon this structure the part is then built. This reduces the stresses that arise from the thermal expansion and minimizes diffusion from the base plate into the part. In addition, the rapid solidification and simultaneous cooling in the process can also lead to intrinsic stresses. Therefore, the entire building chamber is held at elevated temperatures, which allows a stress relaxation within the material to take place. This is usually done by preheating the powder material using the electron beam and heating the base plate [1].

The described process was invented by ARCAM AB, Sweden, and commercialized in 2001. While it was originally only employed for the processing of steel powders, in recent years a wider spectrum of materials has been used [1].

2.2.1 Process Parameters

Many different parameters can be adjusted to optimize the process for each build job individually. Not all of them can be mentioned here, however, the most straightforward regarding the building process itself as well as the precursor powder are described:

Parameters regarding the building process are mostly related to the electron beam itself. These are used to optimize the energy input into the material, where an acceptable balance between good dimensional accuracy and low defect population density occurs. This input is adapted to suit the used alloy composition, the layer thickness and the sample geometry. The inten-

sity of the electron beam is influenced by the beam current I and acceleration voltage U. The electron gun, which usually is a heated tungsten filament, is used to adjust I, which is usually set between a value of mA to A, depending on the individual process. By changing U of the system the final energy of the impacting electrons is set, commonly a value of around 60 kV is chosen. The spot size is defined by adjusting the electromagnetic lensing system. For the heating passes, the electron beam is defocused by adjusting the same lensing system to give as much uniform heat flow as possible on the surface. This causes the powder to sinter a bit, which is favourable in terms of the conductivity of the material, reducing the energy required during the melting step and helping to maintain the high temperatures in the build chamber, which are required to keep the residual stresses in the finished parts at acceptable levels [1]. Improving the conductivity is important in order to reduce the probability of smoking phenomena, which occur when an electrostatic charge causes powder particles to be ejected from the powder layer [21, 22]. During the melting step the beam is focused and scanned across the surface. The scanning speed (v) refers to the velocity of the spot across the surface and strongly influences the energy input. The scanning speed and electron beam power are key factors in terms of the part quality [22].

The hatching strategy is the way the electron beam is scanned across the surface of the powder and includes a set of subparameters. One of them is the way the scan pass is directed across the powder. A common way to do this is to first melt along a contour around the area to be molten and then fill out the rest. This filling-out is often done by moving the spot forward and backward along a line across the surface while incrementally changing the position of the line, which is commonly referred to as a "snake-strategy". It is also possible to scan forward only and then to reset the position of the spot or to apply a spot melting technique where the beam is focused on different points in the area without following a continuous line. The spacing by which the position of the line is shifted with each pass is also part of the hatching strategy. Usually the direction of the melting pass is the same within a layer but changes between the different layers by a defined angle. This is done in order to reduce residual stresses within the finished part [1, 23].

The parameters regarding the powder are its size and size distribution as well as the shape of the particles which all have an influence on the flow properties. Good powder flow characteristics facilitate the introduction of a new powder layer into the build chamber, while bad flow properties do not only impede this process, but can also lead to increased shearing forces between the new powder and the already built part [24]. Flow instabilities in a melt pool can lead to a break up of thin melt pools into spherical droplets, called balling. This effect is commonly described in terms of Rayleigh instabilities [25, 26]. The height by which the build plate is lowered by each step, which is equal to the thickness of the powder layers introduced, is important to consider. Larger steps can increase the build speed. However, the increased amount of pow-

der necessitates an increased energy input which means either higher acceleration voltages or beam currents or a lower scanning speed [1, 27].

2.2.2 Solidification of TNM after Electron Beam Melting

As described in section 2.1.4 TNM solidifies via the β-phase. Upon adding a new powder layer, the electron beam melts the material. The energy input also heats up material beneath that top layer. This increase in temperature results in a local shift to the β+L phase field. The cubic structure of β means that the crystallization occurs preferentially in the <100>-directions along the highest thermal gradient. When cooling the solidification occurs mainly on already existing β-crystals, i.e. at the bottom of the melt pool. The energy introduced into the material has two ways to be transferred away from the melt pool. Either through heat flow towards the solid material or through the free surface. The heat flow through the material results in the material solidifying along grains where the <100>-direction is oriented in the building direction. This causes a β-texture in the final parts.
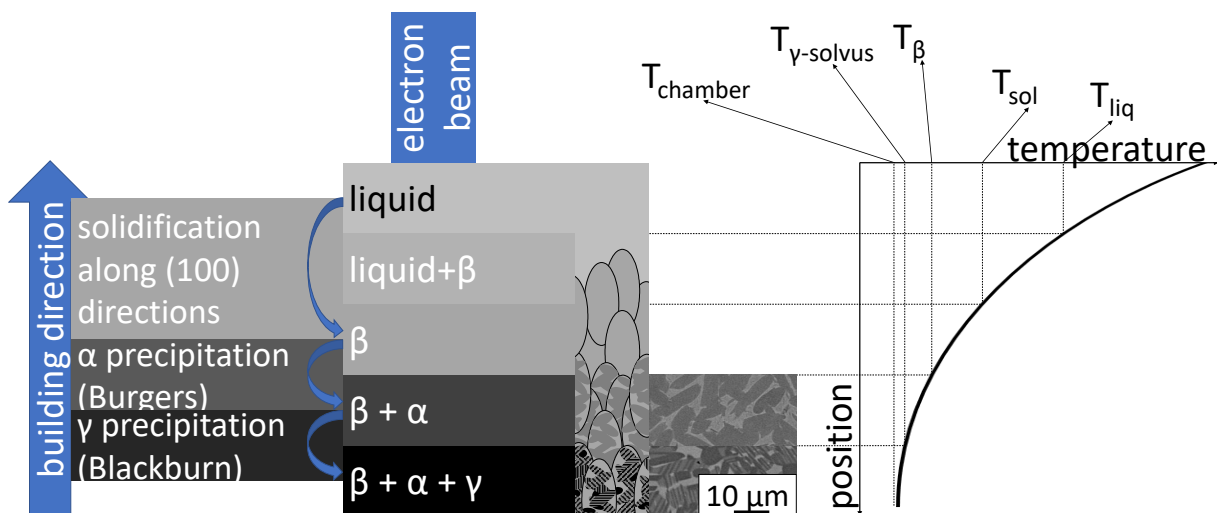
Figure 2.5: Solidification and cooling of the TNM alloy within the EBM machine. The different phases are shown as they occur at different positions within the built material during the EBM process. At the top the electron beam melts the material and lifts it above the liquidus temperature (T_{liq}), below the two-phases liquid and β are stable. After complete solidification below the solidus temperature (T_{sol}) the phase changes occur corresponding to the process described in section 2.1.5. Exemplary SEM-images for the $β_o+α_2$ and $β_o+α_2+γ$-phase areas are given. The $β_o+α_2$-state was obtained by annealing at 1270 °C for 1 h and subsequent air cooling (AC), the $β_o+α_2+γ$-state is visible in the as-EBM material. For the sake of clarity the different phase areas are displayed equal in size, this is not an accurate approximation, the same goes for the different transition temperatures.

Further cooling leads to the precipitation of α/α$_2$ and γ according to the process described in section 2.1.5. This is shown schematically in figure 2.5. Such grain orientations have also been observed in other β solidifying Ti-alloys, for example in Ti-6-4 by Mahbooba et al. [16] and Antonysamy et al. [28]. Until the build job is finished the build chamber is held at about 1100 °C. No major phase changes are expected in this temperature range when considering the phase diagram (figure 2.3).

2.2.3 Aluminium Loss

The high energy of the electrons impacting the material, as well as the high temperatures of the melt pool can lead to partial vaporization of the lighter elements due to their higher vapour pressure. While the heavier elements Mo and Nb are largely unaffected by this, the problem is relevant when considering the loss of Al as an important α-stabilizing element. Schwerdtfeger and Körner [29] have found a correlation between the Al-loss and the energy input of the electron beam for another γ-based TiAl-alloy (Ti - 48 Al - 2 Cr - 2 Nb in at.%, commonly known as the "GE-alloy"). The measure of energy input used was its line energy (LE), a function of the current I, the acceleration voltage U and v. By lowering it they achieved a decrease in Al-loss:

$$LE = \frac{IU}{v} \tag{2.4}$$

This Al loss leads to chemical inhomogeneities within the layers with higher losses at the top of the layer, where the Al-vaporization occurs easily and lower losses at its bottom. A qualitative representation of this can be seen in figure 2.6. In order to minimize the chemical inhomogeneities the line energy can be reduced. However, too little energy input lowers the adhesion between the layers [29, 30].
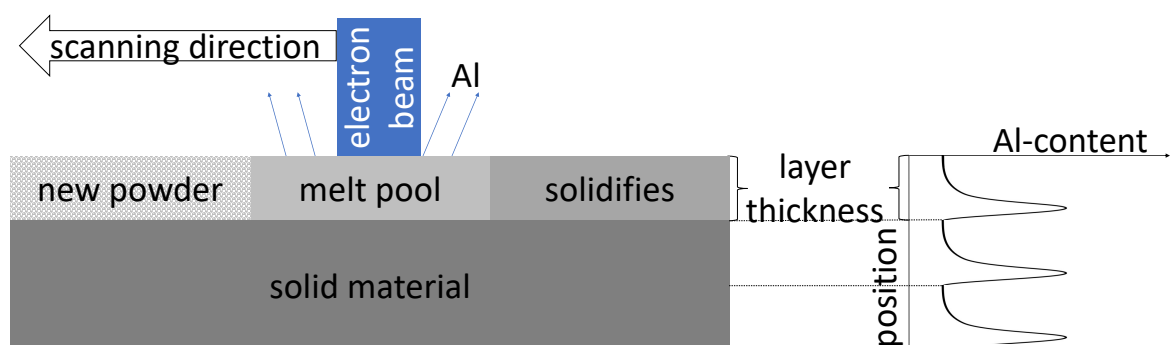
Figure 2.6: The impact of the electron beam results in a higher Al-loss at the top of the melt-pool. At the bottom of the melt-pool this loss is significantly lower, which results in a changing Al-concentration along the building direction.

Another way of reducing these changes might be an annealing step which enhances a balancing diffusion process. A decrease in the Al concentration also means that the β-phase is stable over a larger temperature range which impedes the adjustment of an optimal microstructure since its low-temperature equivalent β_o is generally considered detrimental to the material properties, the causes of which are described in section 2.1.5.

3 Experimental

## 3.1 Samples

3.1.1 Powder

The powder was produced by vacuum induction melting and inert gas atomization (VIGA) by LPW Technology Ltd. (United Kingdom). In this method the material is refined using a vacuum induction melting (VIM) furnace. The material is then poured through a tundish system into a gas nozzle where an inert gas (in this case Argon) is used to disintegrate the melt. During the flight the material solidifies which results in a highly spherical powder [31]. After the atomization the powder was sieved. The powder fraction between between 45 µm and 150 µm from both batches was used in the EBM process.

A powder fraction analysis was executed at the Chair for Process Technology and Industrial Environmental Protection, Montanuniversität Leoben using laser diffraction on a HELOS RODOS by Sympatec GmbH (Germany).

3.1.2 Electron Beam Melting

Cylindrical parts were fabricated from this powder. These had a diameter of 12 mm and a length of 90 mm. Their orientation on the build plate was varied from $0°$ (lying down), to $45°$ and $90°$ (standing upright). A schematic representation of the sample orientations is given in figure 3.1. The parts were manufactured by Neue Materialien Fürth GmbH (Germany) using an Arcam A2X. The following building parameters were used:

- constant LE
- snake hatching strategy with a line distance of 0.1 mm
- the time it takes for the spot to reach the same X-position (return time) during a melt pass for an area is held constant
- 60 kV acceleration voltage
- variable v and I to achieve a constant LE and return time
- temperature of 1050 $°$C in the build chamber
- lowering of the platform with each step of 100 µm
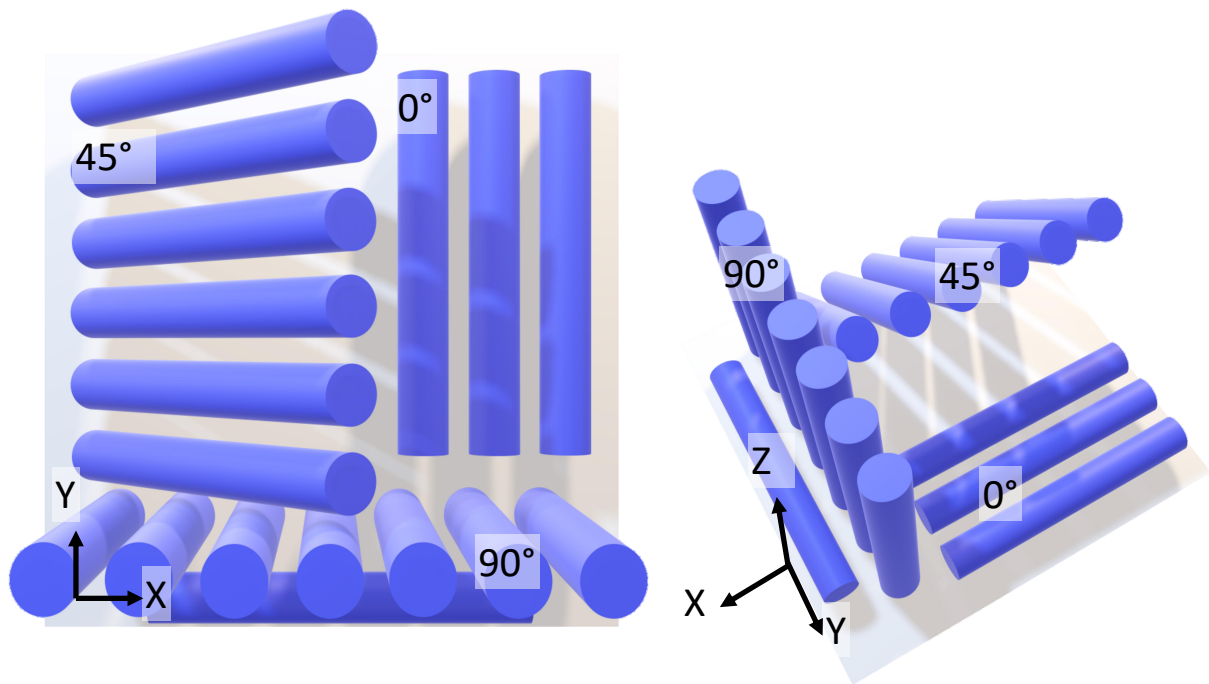
Figure 3.1: Left: Sample orientation as seen from above. **Right**: Sample orientation as seen in an central projection. The designations as used in this thesis are indicated.

3.2 Heat Treatments

In order to gain insights into the change in chemical composition as a result of the EBM-process various samples were annealed. To that end parts were cut from the original cylinders at a length of about 1 cm and annealed for 1 h at various temperatures. The annealing temperatures were chosen over a range from 1200 to 1290 °C in steps of 10 °C with one sample for each temperature. Cooling occurred in air until the samples reached RT. Due to the relatively fast cooling the resulting microstructure was close to that at the respective annealing temperature. These annealing steps provided an insight into $T_{\gamma\text{-solv}}$. Lower Al-concentrations cause a decrease of this temperature (see the phase diagram in figure 2.3), thus allowing an estimate of the changes in chemical composition. $T_{\gamma\text{-solv}}$ is also of practical importance when adjusting the final microstructure of the material [8]. These heat treatments were conducted by MTU Aero Engines (Germany).

3.3 Differential Scanning Calorimetry

In order to perform a thermal analysis a differential scanning calorimeter (DSC) of the type SetaramLabsys evo by Setaram (France) was used. The aim was a measurement of the phase transition temperatures, which can also provide insight into the chemical composition of the

material. This effect is especially pronounced with respect to the Al-loss, as small changes in concentrations can cause strong shifts in $T_{\gamma\text{-solv}}$ and T_β. Their values are also important when choosing adequate heat treatments.

The investigated samples were taken from one of the 45° build orientation EBM parts, powder in the as-atomized state as well as powder that was recovered from the build chamber after the EBM-process. A sample of roughly 100 mg was placed in an Al_2O_3-crucible and then heated under an Ar atmosphere. The heat flow was measured as a function of temperature, and any deviations from the sample crucible to a second reference crucible were recorded. These relative differences in heat flow were then used to evaluate phase transition temperatures, which show in the form of peaks. During heating a thermodynamic equilibrium is never achieved and the temperatures of the phase transitions are shifted towards higher values. Therefore, the curves were measured for heating rates of 10, 20 and 40 K/min. Then a linear extrapolation of the heating rate was calculated to estimate the phase transition temperatures at 0 K/min, which is equivalent to the thermodynamic equilibrium. For a further description of DSC and the methods used here the reader is referred to Böck [32] and Menczel et al. [33]. Sample curves for the heat flow curve as well as the linear extrapolations are given in figure 3.2. All evaluations of the data were executed using OriginLab 2017.

3.4 X-Ray Diffraction

In order to determine the phase fractions of the α_2-, β_o- and γ-phases X-ray diffraction (XRD) patterns of different samples were measured using a Bruker D8 Advance. The peaks in these patterns can be attributed to the respective phases in the material. The samples investigated were the as-atomized powder, powder recovered from the build chamber as well as as-EBM material from each build orientation. Patterns from the heat treated samples described in section 3.2 were also collected.

The X-ray radiation was Cu-K_α which corresponds to a wavelength λ of 1.54 Å, the spectrum was measured between the angles 2θ of 11° and 82° in increments of 0.02°. In the case of polycrystalline material, i.e. EBM samples the samples were rotated during the measurement in order to gain a better statistical estimate. For the powder this was not necessary. A sample pattern with the peaks corresponding to the relevant phases is given in figure 3.3. Rietveld refinements were executed to evaluate the gained data with respect to the relative phase fractions. The software used to do this was Topas (Version 4). A Rietveld refinement uses the known crystallographic data of the individual phases to fit an entire pattern. For a more detailed description of the Rietveld refinement the reader is referred to [34].
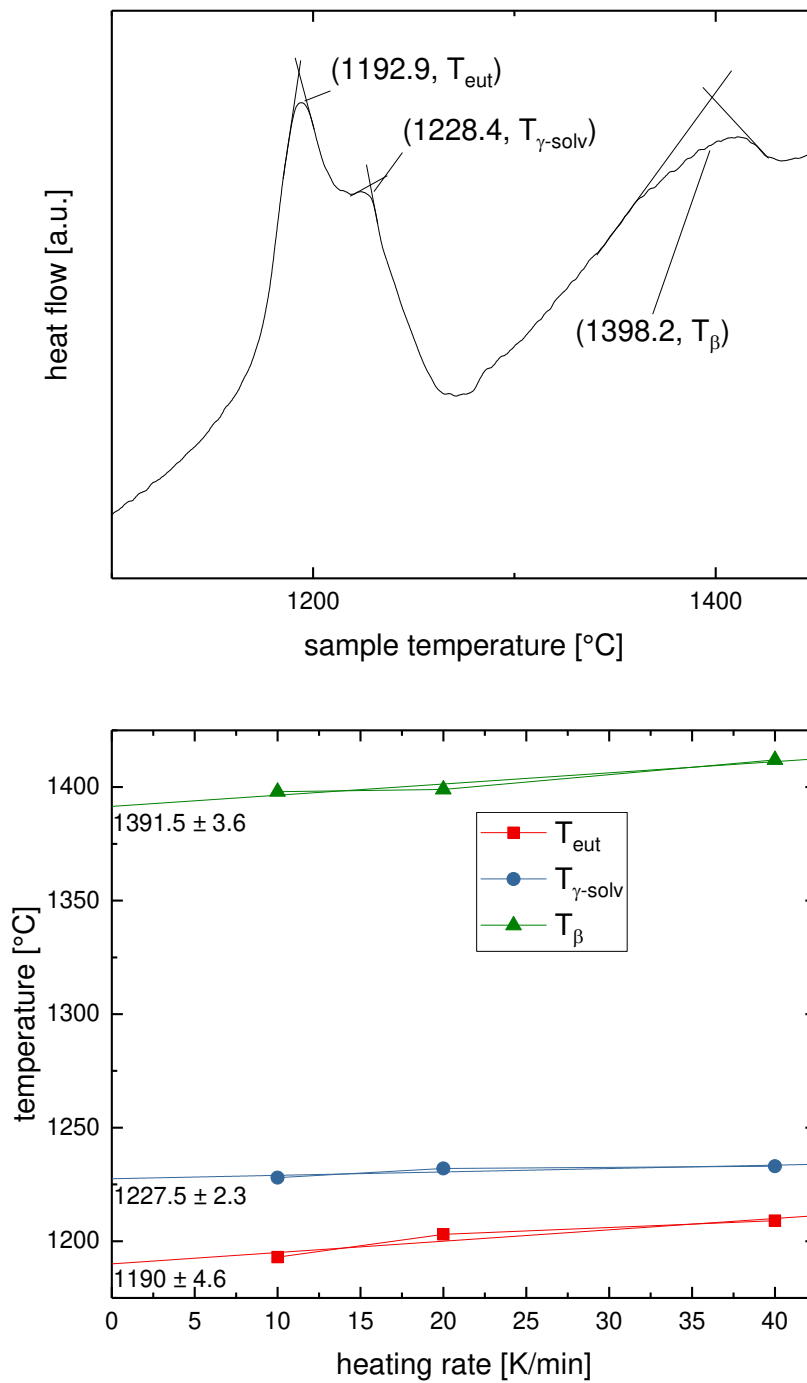
Figure 3.2: Top: DSC curve as measured for an as-EBM (45° build orientation) sample at a heating rate of 10 K/min with the different transition temperatures indicated. **Bottom**: Extrapolation of the measured transition temperatures towards 0 K/min.
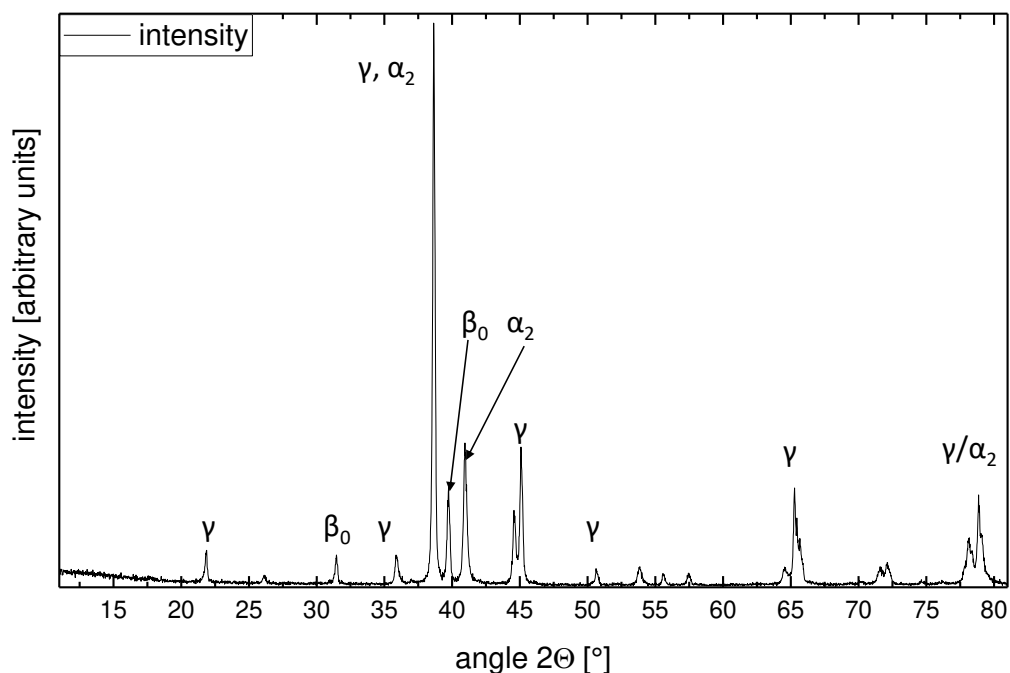
Figure 3.3: Diffraction pattern of the TNM powder after being recovered from the build chamber. Peaks corresponding to all the prevalent phases in TNM are visible.

3.5 Microscopy

The microstructure was evaluated using different microscopical methods. Unless otherwise specified the samples were prepared by grinding, using sandpaper up to a grit of 4000, then polished using 3 μm and 1 μm diamond suspension for about 2 min each. Finally they were polished using an oxide particle suspension (OPS) for about 10 seconds.

3.5.1 Light Optical Microscopy

The light optical microscope (LOM) used was a Zeiss Axio Imager M1m with the software Axio Vision V4.8.2.0. After the sample preparation as described in section 3.5 an additional etching step was executed in order to reveal the microstructure for LOM investigations. This was done using the method described by Ence and Margolin [35] on a Struers Lectropol-5. The etching parameters were 5 s, a voltage of 45 V and a flow rate of 8.

Stereomicroscopical images were taken using a Zeiss Stereo Discovery.V20. The software for this microscope is the same as for the optical microscope. Both microscopes used the software AxioVision V 4.8.2.0.

3.5.2 Scanning Electron Microscopy

The scanning electron microscope (SEM) used for the back-scatter images and the energy dispersive X-Ray spectroscopy was a Zeiss Evo 50 with a LaB_2 field emission cathode. All SEM images provided in this work were obtained using the back-scattered electron (BSE) contrast unless otherwise specified.

For electron back-scatter diffraction (EBSD) an SEM of the type Versa 3D HiVAC with a LaB_2 field emission cathode was used. The software employed to evaluate the EBSD images was TSL OIM Analysis 7. For this evaluation several clean-up steps were required. These included the omission of individual pixels whose orientation and/or phase differed from the surrounding material. An orientation clean-up was executed, which merged grains when their difference in orientation was below $5°$. Using the same software pole figures were calculated. These show the grain orientation as well as the orientation relationships described in section 2.1.5.

For EBSD the samples should be under little or no mechanical stress, because even small forces can distort the unit cells of the material and thereby reduce the quality of the measurement. To achieve this the samples were ground using sandpaper up to grit 4000, followed by a polishing step using 3 µm diamond suspension for 20 seconds and OPS for 10 seconds. Afterwards the samples were vibropolished for 1 h using a mixture of 50 % alcohol and 50 % OPS. The phases measured were α, β and γ.

3.6 Phase Analysis

The phase analysis of the micrographs obtained via LOM and SEM was executed using the software Stream Motion 1.9.3 by Olympus (Japan). In order to improve the visibility of the phases the images were adapted to improve their contrast, sharpening and blurring filters were also applied. While the EBSD measurements could also have been used for a quantitative phase analysis they were discarded in this context, as the clean-up-operations executed changed the results strongly. The measured areas in EBSD were relatively small which would mean the data may not be statistically valid, further decreasing their value for phase analysis.

In the LOM as well as SEM images the $β_o$-phase shows the lightest and the γ-phase the darkest contrast. In the LOM micrographs discerning the $β_o$- and $α_2$-phase was difficult. Therefore these phases were often not distinguished and the combined phase fraction of $β_o + α_2$ evaluated. An example of the phase analysis using an SEM-image, showing the different steps, is provided in figure 3.4.
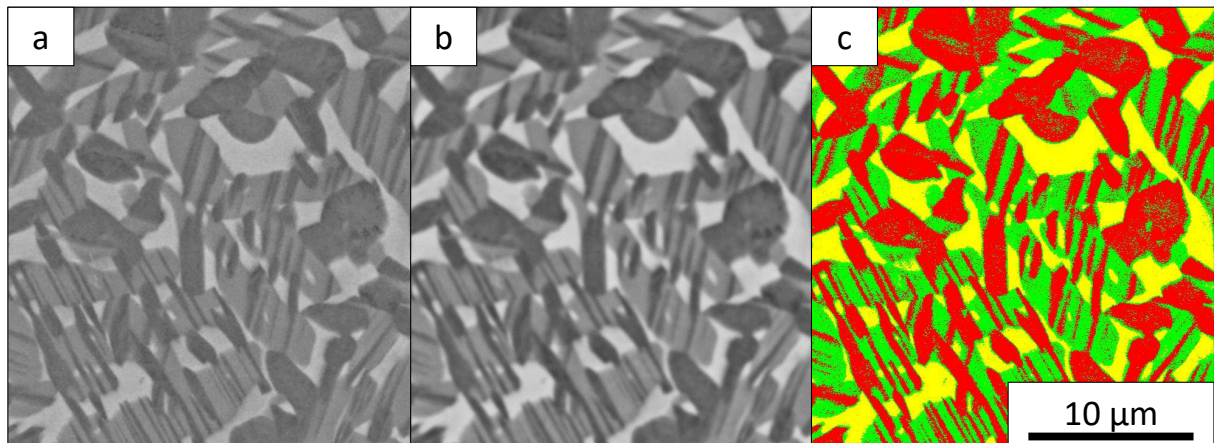
Figure 3.4: Phase analysis of a 90° build orientation as-EBM sample. This sample showed a triplex (α_2+β_o+γ) microstructure. **a**: Original SEM-image. **b**: Image after improving contrast and applying sharpening and blurring filters. **c**: The phase fractions are color coded and according to the evaluations they are: green-α_2 (35 vol.%), yellow-β_o (19 vol.%), red-γ (46 vol.%).

3.7 Chemical Analysis

The chemical analysis of powder and as-EBM samples was executed at the Gesellschaft für Elektrometallurgie (Germany). It was conducted to evaluate the overall Al-loss as well as other possible changes in the chemical composition. Several methods were used, dependent on the different elements measured: The main elements were detected using X-ray fluorescence analysis (XFA), impurities using atomic emission spectroscopy (AES) and gases as well as C using LECO-combustion (named after the company LECO, USA).

3.8 Mechanical Tests

Prior to mechanical testing the samples were hot isostatically pressed (HIPed) under a pressure of 100 MPa at 1200 °C for 4 h and slowly furnace cooled (FC), to achieve a NL+γ-microstructure. In order to get a NL+β-microstructure two additional heat treatment steps were executed: First a step at 1290 °C for 30 min with air cooling (AC) and then at 850 °C for 6 h with FC. Tensile tests were conducted on both types of adjusted microstructure, creep tests only on NL+β-samples.

During the annealing process for the 0° NL+β-microstructure an error occurred. These samples were left in the furnace for an extended period of time (several h, the exact time is unknown) at 1290 °C and then cooled down slowly. In order to achieve the closest microstructure possible relative to the intended one annealing steps were repeated from the beginning. However, it is likely that the microstructure has been significantly changed. Since no direct comparison was

possible due to a lack of equivalent samples no further investigations into these differences were performed.

3.8.1 Tensile Tests

The tensile tests were executed at MTU Aero Engines, Munich, Germany according to the internal norm MTL 166-3. Prior to measuring the samples were annealed to achieve both NL+γ- and NL+β-microstructures. The stress strain curves were measured at different temperatures, a complete test matrix of all the measured samples is given in table 3.1. The tests were executed at RT, at 300 °C and at 750 °C under a constant strain rate of $5 \cdot 10^{-5} s^{-1}$. Temperature control occurred using 3 thermal couples of type B at different positons along the sample. Due to a shortage of testing material not every build orientation could be tested at each temperature.

The sample geometry had an original gauge length of 25 mm, a diameter of 5 mm and a

Table 3.1: Tensile tests were executed for samples of all orientations at RT, 300 °C and 750 °C. The microstructures were NL+β and NL+γ

sample orientation	microstructure	test temperature [°C]	Nr of samples
0°	NL+β	300	1
45°	NL+β	RT	1
45°	NL+β	300	2
90°	NL+β	RT	1
90°	NL+β	300	2
90°	NL+β	750	1
0°	NL+γ	300	2
45°	NL+γ	300	2
90°	NL+γ	300	2

.

threaded head of type M10. The testing station was an Inspekt 100 made by Hegewald & Peschke Mess- und Prüftechnik GmbH (Germany) equipped with a furnace made by Könn GmbH (Germany). The change in length was measured using an high temperature extensiometer of type PMA-12/2/V7 by Maytec Mess- und Regeltechnik GmbH (Germany).

3.8.2 Creep Tests

The creep tests were executed at MTU Aero Engines (Germany). A testing station of type Roell/Amsler equipped with a furnace made by Heraeus Holding GmbH (Germany) was employed to test samples of the same geometry as for the tensile tests (see section 3.8.1). The

strains were measured with an extensiometer made by Dr. Johannes Heidenhain GmbH (Germany). For temperature control 3 type B thermal couples and a modulator made by JUMO Mess- und Regelgeräte GmbH (Austria) were used. The test duration was roughly 1000 h at a temperature of 750 °C and a stress of 150 MPa. This was done in order to measure the minimal creep rate for each of the samples. Prior to testing the samples were annealed in order to achieve a NL+β-microstructure. One sample of each build orientation was used to gain the strain-time curves.

The obtained strain (ε) vs. time (t) curves were fitted in OriginLab 2017 using a function based on the works of Garofalo [36] of the form:

$$\varepsilon = a \cdot (1 - \exp(-b \cdot t^{1/2})) + c \cdot t + d \cdot \exp(e \cdot t^f - 1) \qquad (3.1)$$

where the term $a \cdot (1 - \exp(-b \cdot t^{1/2}))$ is used to fit the primary creep, the linear term $c \cdot t$ to describe steady state creep and $d \cdot \exp(e \cdot t^f - 1)$ to fit tertiary creep with the parameters a to f being used to optimize the fit. The equation was implemented with the user defined fit function, the convergence limit was set at a relative change of the fit of 10^{-15} or until the software could no longer improve the fit. For a better approximation of the onset of creep the parameters for the onset and stationary creep were calculated first, while leaving the others fixed. After this step all the parameters were fitted.

In order to find the strain-strainrate curves and the minimum of the creep strain rate $\dot{\varepsilon}$ the derivative of ε with respect to time was numerically calculated. An example of the strain vs time and strain vs strain rate curves is provided in figure 3.5. For LOM analysis the samples were cut along the testing length and then prepared as described in section 3.5. Since the original sample orientation in the build chamber was no longer discernible the cut was made arbitrarily, only for the 90° build orientation the viewing direction can be considered equivalent to those obtained previously from the as-EBM specimens.

3.9 Deformation Dilatometry

In order to evaluate the deformation behaviour of the EBM material samples were deformed at around 1200 °C using a deformation dilatometer of the type DIL 805 A/D made by Bähr (now owned by TA Instruments, USA). The aim was to measure true stress (k_f) - true strain (φ) curves on as-EBM material as conducted by Werner et al. [12]. Therein cylindrical samples of length 8 mm and diameter 4 mm were tested. A thermal couple attached to the specimen was used in a feedback loop to control the temperature. The sample was positioned between two punches at the centre of an inductive coil. First the test chamber was evacuated until the pressure reached $3 \cdot 10^{-6}$ b. Then the coil was used to heat the sample at a rate of 1200 K/min. After being held for five min at the desired temperature the sample was deformed between the
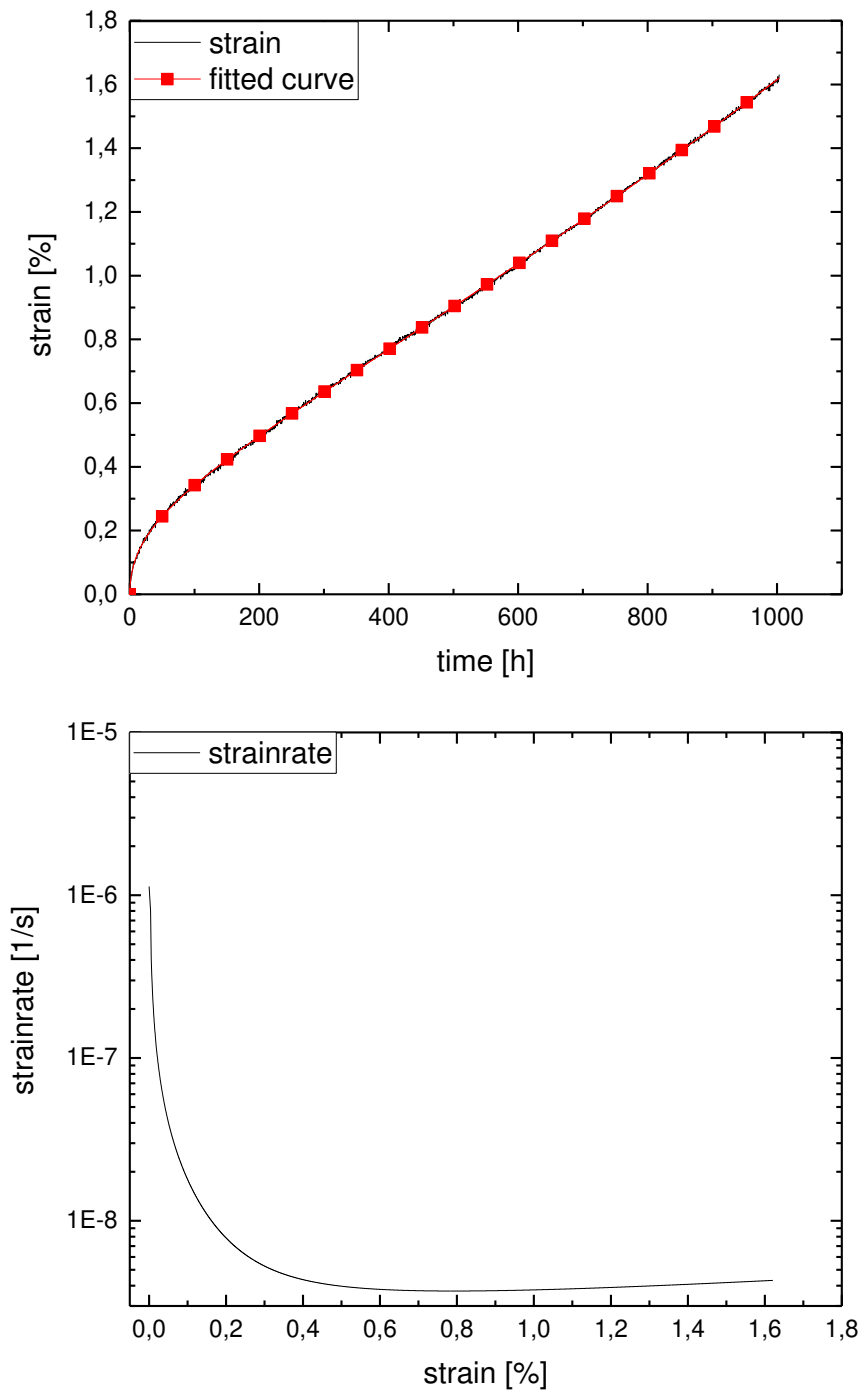
Figure 3.5: Top: Original measured data of the sample at 45° build orientation and the fit as calculated in OriginLab2016 according to equation 3.1. **Bottom**: Strain rate vs strain curve.

punches. The deformation was conducted using logarithmic strain rates $\dot{\varphi}$ of 0.5 s^{-1} and 0.05 s^{-1} (only 0.5 s^{-1} in the case of the 45° orientation) up to a true strain φ of 0.4. After deformation the sample was quenched using N_2-gas. The system was controlled using the internal software package WinTA. The thermal couple used was of type B. This couple contained Pt, an element which forms a eutectic with Al [37]. In order to avoid the resulting low-melting phase a thin Ta sheet was attached to the samples using a spot welding machine of type Spot Welding Fixture 9061 (also made by Bähr) under a stream of N_2-gas. The thermal couple was attached using the same spot welding machine.

4 Results and Discussion

4.1 Chemical Composition

The EBM-process resulted in a loss of lighter elements, in this case in particular Al. These changes in chemical composition are of prime interest as they influence the properties of the material. In table 4.1 the changes in composition of as-atomized powder, powder recovered from the build chamber and as-EBM material are compared. As can be seen the powder composition is close to the nominal composition of TNM in both cases, although the O-content was increased in the recovered material. The Al-content in the as-EBM material is lowered by over 1 at.%. This loss is comparable to that measured by Schwerdtfeger and Körner [29], they managed to decrease this effect by adapting the beam strategy. When considering the phase diagram in section 2.1.4 it is apparent that the decreased Al-content, in the as-EBM material as well as any samples subsequently fabricated, has an increased β-fraction when compared to nominal TNM. The fact that the powder showed almost no change in composition indicates that the preheating passes did not have sufficient energy to cause Al-loss. During the melting step on the other hand the LE is high enough to cause significant Al-evaporation.

Table 4.1: Chemical composition of powder and as-EBM material compared to the nominal TNM composition. The measurements were conducted at the Gesellschaft für Elektrometallurgie, Germany. The rest to 100 at.% is made up by other elements.

material	Ti	Al	Nb	Mo	B	C	H	N	O
					elements [at.%]				
Powder as-atomized	51.12	43.40	4.05	1.01	0.10	0.01	0.04	0.07	0.14
Powder recovered	51.04	43.43	4.03	1.01	0.10	0.01	0.04	0.09	0.28
as-EBM 45°	52.25	42.02	4.12	1.03	0.10	0.01	0.04	0.10	0.20
as-EBM 90°	52.20	42.05	4.11	1.01	0.10	0.01	0.04	0.10	0.22
nominal composition	51.4 (rest)	43.5	4	1	0.1	-	-	-	-

The transition temperatures evaluated by thermal analysis showed a trend that agreed with these findings. As shown in table 4.2 both $T_{\gamma\text{-solv}}$ and T_β are significantly lowered in the as-EBM sample relative to the powder. This is an effect of the decreased Al-content, as evident when considering the phase diagram in section 2.1.4.

Table 4.2: Transition temperatures as found by evaluating DSC-curves of powder in the as-atomized and recovered state as well as an as-EBM sample. For 10K/min the T_β in the powder could not be reliably estimated from the curves, thus the errors are unknown and larger than those of the as-EBM sample.

|	temperatures [°C]		
sample	$T_{eutectoid}$	$T_{\gamma\text{-solv}}$	T_β
EBM 90°	1190±4.6	1227.5±2.3	1391.5±3.6
powder new	1187±1.3	1255±3.9	1382
powder old	1198.5±0.3	1260±0.7	1363

4.2 Powder Analysis

As described in the previous section the as-atomized powder as well as the powder recovered from the build chamber had a composition close to the nominal TNM-alloy. While the chemical composition changed little as a result of the EBM-process, XRD-analysis revealed that the phase fractions did. The as-atomized powder exhibited only α_2 and β_o-peaks. This is due to the fast cooling conditions of up to 10^5 K/s during the powder production that result in a microstructure far from the thermodynamic equilibrium [31, 38]. The high temperature in the build chamber caused a shift towards the equilibrium phase constitution, leading to the precipitation of γ. The phase fractions as calculated by Rietveld analysis can be seen in table 4.3.

Table 4.3: Quantitative phase fractions of the powder as calculated using Rietveld-refinement.

|	phase fraction [vol%]		
sample	α_2	β_o	γ
powder as-atomized	77	21	2
powder recovered	23	7	70

The powder size distributions before and after the EBM process differed strongly. The average particle size shifted towards larger values. As can be seen in figure 4.1 the particle size in the as-atomized powder was strongly bimodally distributed, the recovered material is only very weakly so. This effect is caused by electrostatic forces between particles and containers. Smaller particles are affected more strongly by these forces and therefore tend to remain in their containments [39]. A smaller influence can also be attributed towards the presintering of particles as a result of the heating passes during the EBM process [23].
For a further investigation of the microstructure and morphology of the powder SEM micro-
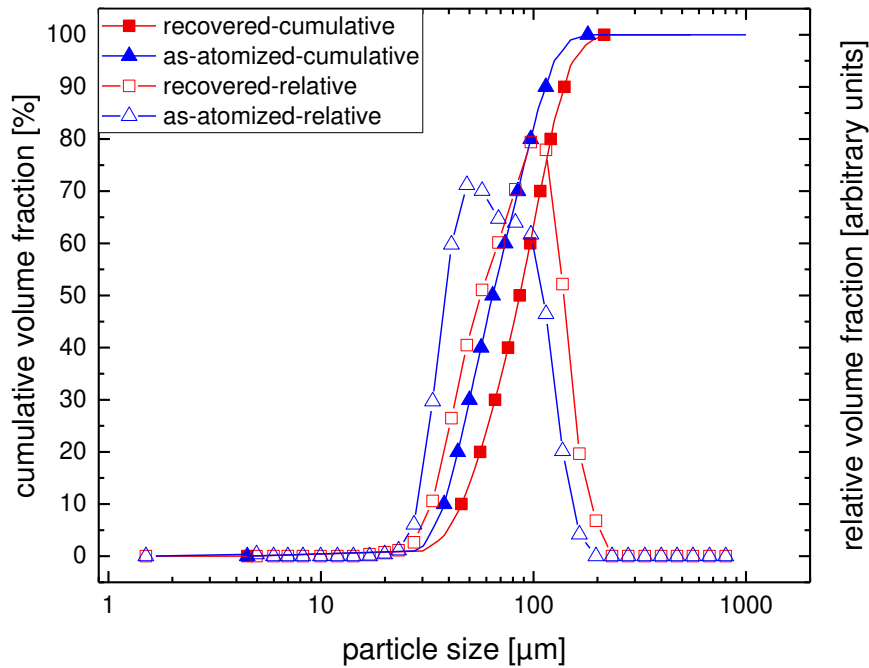
Figure 4.1: The cumulative and relative volume fractions of particles are depicted over the particle size. In both cases the powder shows a bimodal distribution, although this is less pronounced in the recovered powder.

graphs of the powder surface and cross section of particles were made, these are provided in figure 4.2. In the cross section of the as-atomized powder no clear distinction between phases was possible. A change in contrast indicated microsegregations and the surface revealed a dendritic morphology, comparable structures have been found by Kastenhuber et al. [38] in similar powder. The as-atomized material also had some abnormally shaped particles and satellites.

In the powder recovered from the build chamber the phases could be clearly distinguished. This was due to the shift towards thermodynamic equilibrium, and subsequent precipitation of γ also observed using XRD and DSC analysis, while exposed to the conditions in the build chamber. While the particles visible in the micrograph cannot be considered a representative sample for the entire powder the larger average particle diameter in the recovered material was apparent, which conformed with the measurements of particle size distribution. Some sintering also occurred in these particles. The dendritic morphology was less pronounced, as the high temperatures allow for a decrease in surface area to minimize the energy.
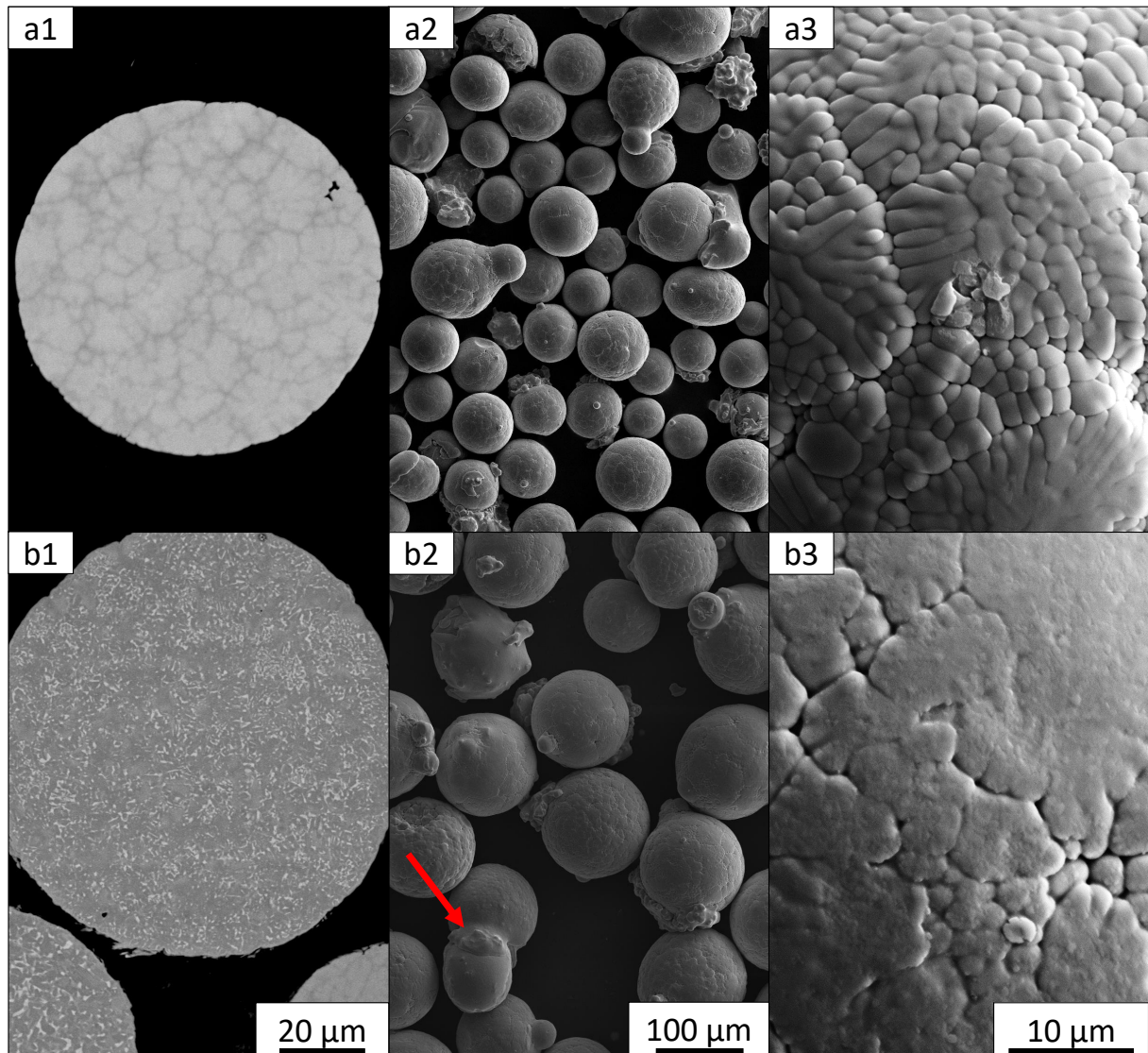
Figure 4.2: The micrographs of the grain surfaces were made using the secondary electrons (SE) contrast. **a1**: The new powder does not allow for a clear distinction between the individual phases, the contrast indicates microsegregations. **b1**: The used powder shows stronger contrasts the phases and allows a distinction between β_o(light) and $\alpha_2+\gamma$-colonies (dark). **a2**: A relatively wide distribution of particle size is visible for the powder, some material shows satellites or abnormal forms. **b2**: The particles in the recovered powder are larger. The red arrow indicates a sinter neck. **a3**: The as-atomized powder exhibits a dendritic surface morphology as also observed by Kastenhuber et al. [38]. **b3**: In the used powder the dendritic morphology is still visible to some degree, although much less pronounced.

## 4.3 Microstructure

4.3.1 General

The samples in the as-EBM state exhibited a triplex $\alpha_2+\beta_o+\gamma$ microstructure as can be seen in figure 4.3. Differences in coarseness and porosity were visible dependent on the build orientation. The 0° build orientation displayed the finest and 45° the coarsest structure. This applied to the lamellar spacing within the $\alpha+\gamma$-colonies as well as the size of the globular γ and β_o. These differences indicate that different cooling rates were present dependent on the build orientation, with the finest microstructure corresponding to the fastest cooling rate. While the SEM images provided a better discernibility of the β_o-phase, in the LOM micrographs the grain boundaries of the original β_o-grains as they grow during the solidification process were still visible. Sample images are provided in figure 4.3, in figure 4.3 a the remaining β_o-phase and an original grain are indicated.
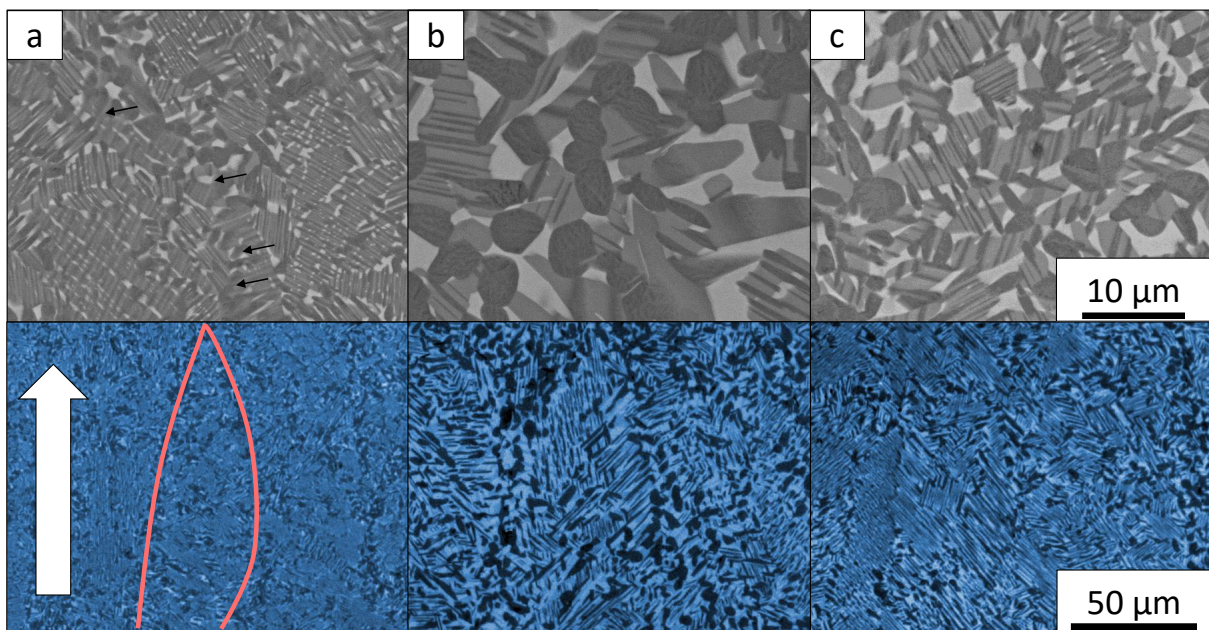
Figure 4.3: Top: SEM images of the three different building orientations. The phases appear as follows: α_2 medium grey, β_o light and γ dark grey. **Bottom:** LOM images of the different building orientations. The arrow indicates the building direction and only applies to the LOM micrographs. α_2 and β_o cannot be distinguished in the LOM images and appear brightly, γ appears dark. **a**: The 0° sample shows the finest microstructure and displays remaining β_o areas within the lamellar colonies which are indicated using the arrows. An original β-grain as solidified as it resulted from the solidification is indicated with the red outline. **b**: The 45° oriented sample displays the coarsest microstructure. **c**: The 90° oriented sample displays an intermediate microstructure.

## 4.3.2 Porosity, Bonding Errors and Layered Structure

As can be seen in figure 4.4 the samples in the as-EBM state exhibited porosity in all build orientations. Pores manifest in the shape of spherical holes in the material, they stem from gas entrapped within the precursor powder [40, 41]. In addition the 0° build orientation also exhibited process related bonding errors. Unlike the spherical pores they were cavities parallel to the position of the layers introduced in the EBM process. Such flaws occur when material is insufficiently molten, which impedes an optimal fusion of the layers [29, 41].
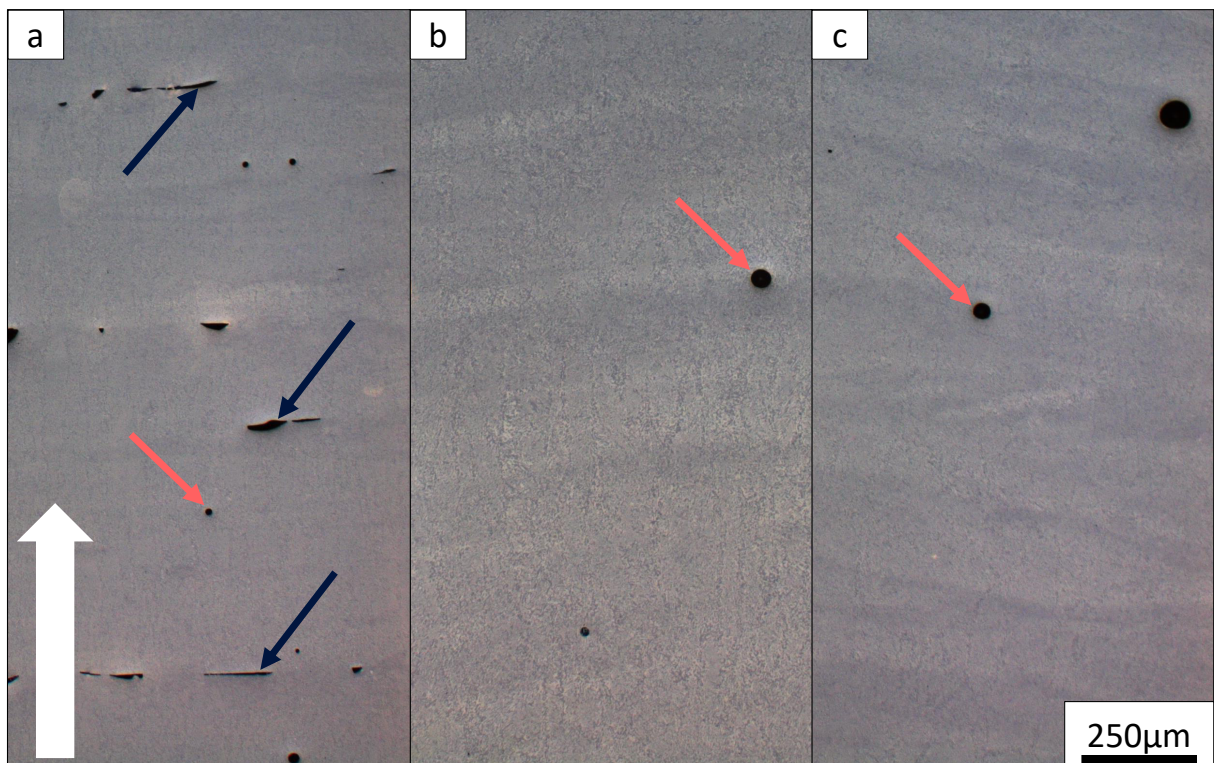
Figure 4.4: LOM images of samples as EBM after polishing and etching. Bonding errors are indicated by the blue arrows, circular powder related pores by red arrows. The white arrow indicates the building direction. **a**: The 0° orientation shows both bonding errors and porosity. **b, c**: The 45° and 90° orientations display only pores. A layered structure is visible for all samples indicating the Al-loss further elaborated on in section 4.3.3. In particular for the 45° orientation the shape of the original β-grains can still be recognized.

These errors resulted from an insufficient LE in combination with the choice of hatching strategy. Figure 4.5 a shows a qualitative depiction of how the electron beam was scanned across the 0° build orientation samples. Alternating between each layer the scanning strategy followed type 1 and type 2. As can be seen the time between reaching the reference position is much longer for type 1 than 2 assuming a constant scanning speed. By changing the EBM

parameters it was attempted to keep this time as well as the LE constant. However, due to technical limitations this was not possible and the scanning speed had to be reduced in order to keep LE at the same level. This means an increased return time, which in turn allows for more heat to be either dissipated through the material or radiated into the build chamber. As evidenced by the bonding errors this loss of heat in turn resulted in a flawed bonding between the layer which is visible in the form of the stretched cavities. As more heat can leave the material, a faster cooling of the subsequently molten layer is expected. This faster cooling then conforms with the finer microstructure of the $0°$ build orientation sample observed in the previous section. However, it does not explain the difference in microstructure between the $45°$ and $90°$ orientation. A different hatching strategy that would likely not result in such a problem is suggested in figure 4.5 c.
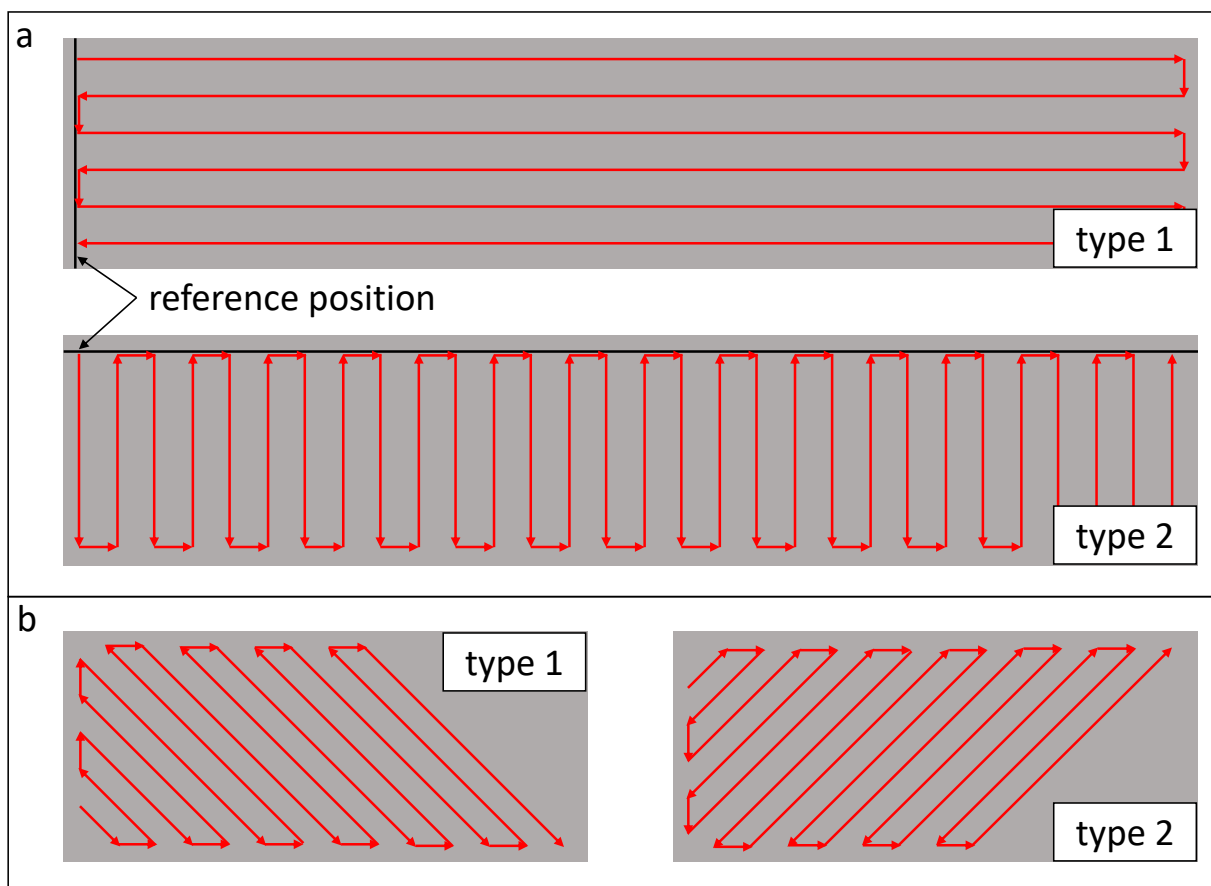
Figure 4.5: The red arrows indicate the direction of the scanning spot over the sample surface indicated in grey. **a**: Alternating between the layers the spot is scanned across the surface in the different directions of type 1 and type 2. **b**: An alternative scanning strategy is to move the spot along lines oriented at an angle of $45°$ to the length axis of the sample. This shortens the time until a reference position can be reached, preventing the sample from cooling too much.

On larger scales a pile-up of material towards the sample centers was visible as indicated in figure 4.6. How this occurred is unclear as, however the trends of increasing pile-up and of coarsening microstructure go in the same direction. A coarser microstructure suggests a higher energy input, while an increasing number of bonding error is a result of a lower energy input, or, as in this case the result of too much heat leaving the sample during the melting step. This suggests, that this pile-up is more pronounced with increasing energy input. Other works have also reported on swelling phenomena of material during EBM as a result of overheated material, although these phenomena were described in terms of their surface effects [42, 43]. Maybe a related effect caused this pile-up in the microstructure.
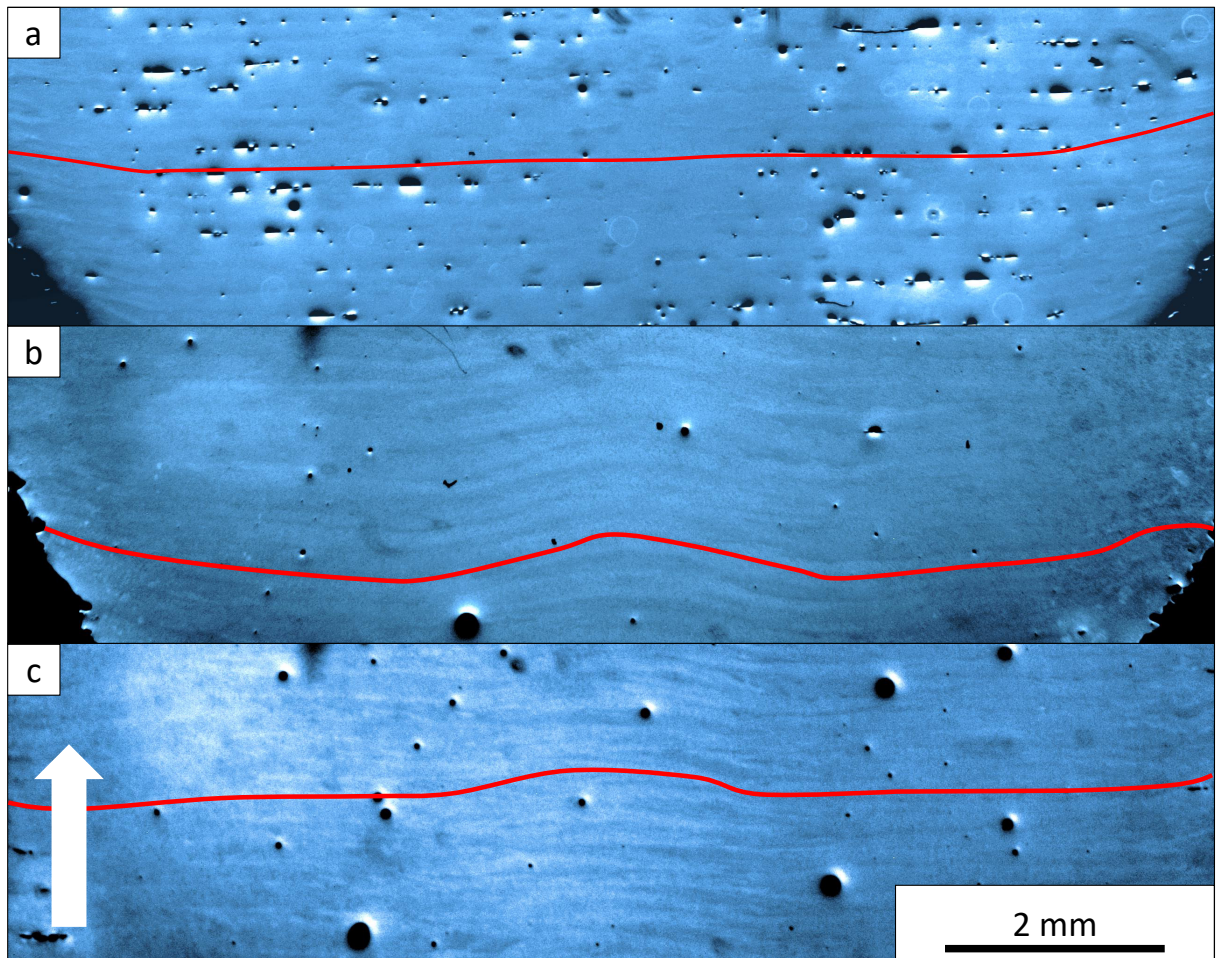

Figure 4.6: LOM images of the as EBM samples show the pile up at the sample centers with the red lines indicating a layer. The arrow indicates the building direction. **a**: The $0°$ orientation shows little to no pile-up. **b**: The $45°$ sample exhibits the strongest pile-up. **c**: At $90°$ some, however only little pile-up is visible.

4.3.3 Al-loss

As described in section 4.1 a decrease in Al-concentration of about 1.4 at.% occurred in the material as a result of the EBM process. LOM images of annealed samples revealed that this loss did not occur uniformly across the material. Figure 4.7 shows different amount of γ-phase in the samples dependent on both annealing temperature as well as position in the sample. This is caused by a locally changing $T_{\gamma\text{-solv}}$, which changes with the Al-concentration. Such inhomogeneities mean that a standard route of EBM + HIP + heat treatment to achieve an optimal microstructure is no longer feasible due to the local shifts of transition temperatures. A diffusion annealing step might help to alleviate this problem.

The model used to describe this local Al-loss is described in section 2.2.3. This model leads to the expectation that the Al-loss occurs with a periodicity of the introduced layer thickness, in this case 100 µm. As figure 4.7 c shows the actual distance is about twice that. Additional investigations would be required to learn why this occurs.
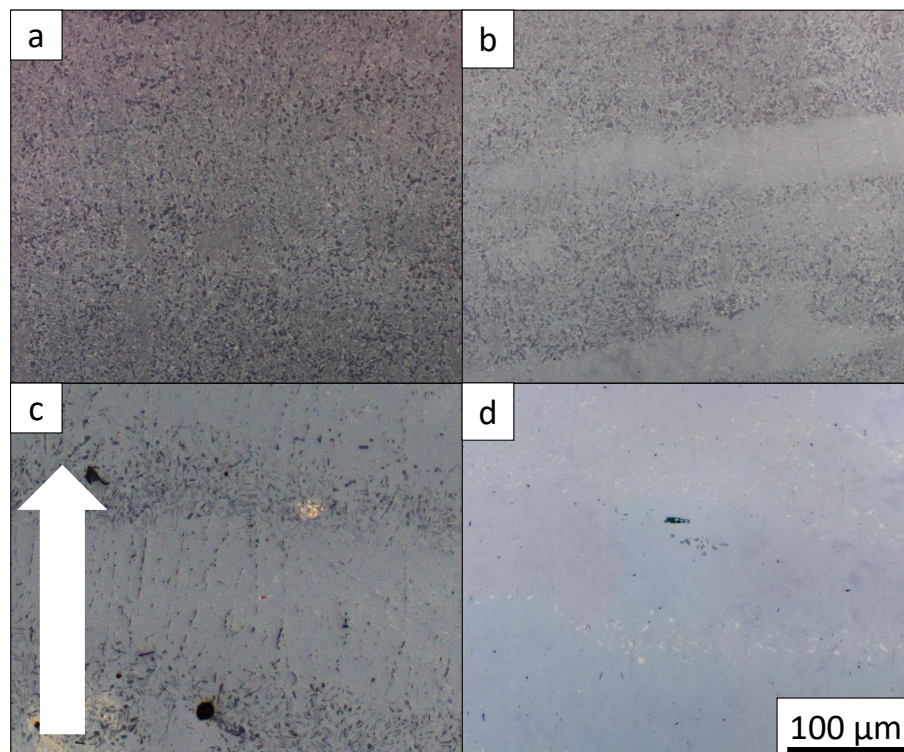
Figure 4.7: LOM images of samples annealed at different temperatures for 1 h and cooled in air. The arrow indicates the building direction. **a**: At 1200 °C the sample orientation of 0° has no large γ-free areas. **b**: After annealing at 1210 °C already some γ-free areas appeared (also for 0° orientation). **c**: For the 45° orientation annealing at 1240 °C resulted in a periodic appearance of γ. **d**: The 90° orientation showed (almost) no visible γ anymore after annealing at 1260 °C.

4.3.4 Texture

The evaluation of LOM and SEM micrographs showed highly elongated grains (compare figure 2.2). This as well as the fact that the alloy solidifies via the bcc β-phase suggested the formation of a texture in the direction of heat flow during solidification. In order to evaluate this texture EBSD investigations were conducted. As some β-phase remained at RT, it was be used to directly investigate the texture of the solidified material. Images of the isolated β-phase and the respective β-(100) pole figures are given in figure 4.8.
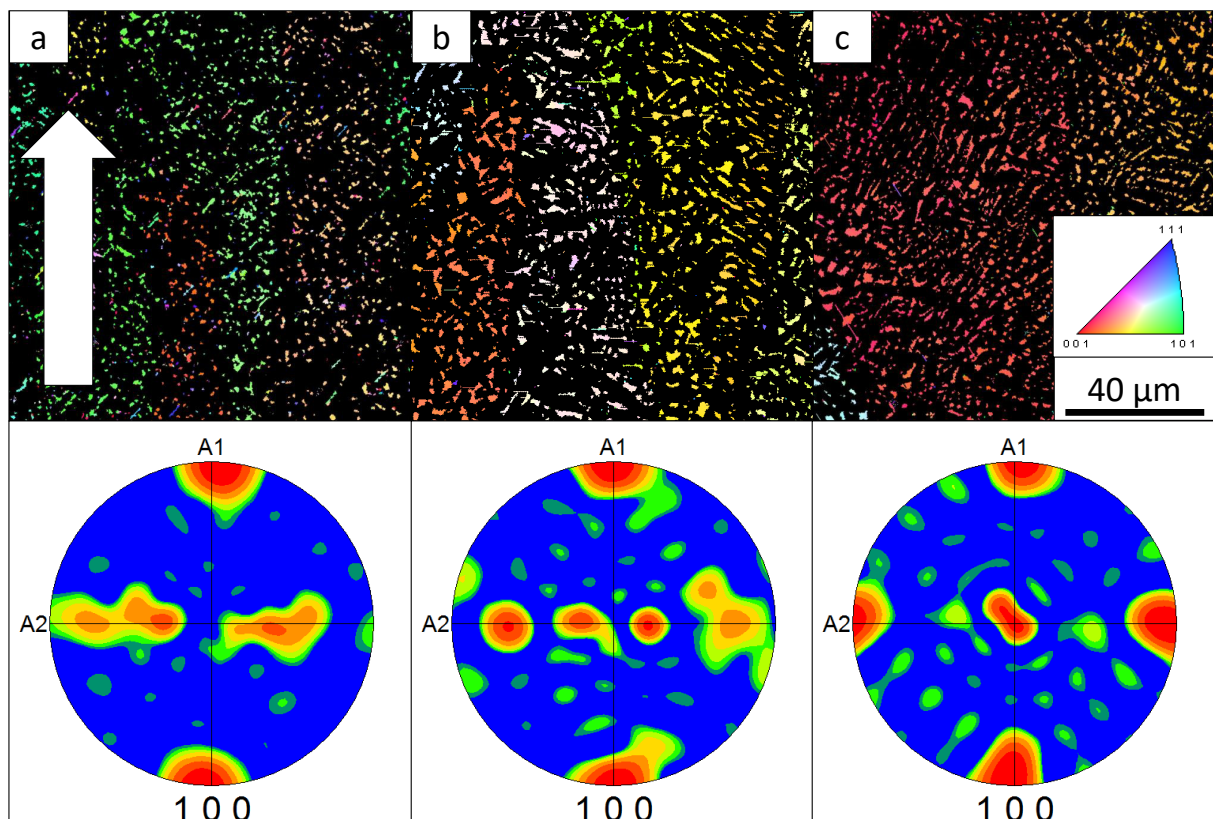

Figure 4.8: The maps and corresponding pole figures of the β-phase for as EBM samples for the three orientations of **a**: 0°, **b**: 45°, **c**: 90°. The arrow indicates the building direction. The pole figures are oriented the same way, which means that A1 corresponds to the building direction.

The pole figures showed the β orientation in the building direction, while no preferred orientation appears to be prevalent perpendicular to it. Similar texture effects have been found in other β-solidifying Ti-alloys [16, 28]. This was strongly visible in the 0° and 45° orientations. For these orientations the elongated grains that were observed in LOM could also be discerned (compare figure 4.3). They had such a high aspect ration that no single grain was visible in it's entirety. The trend in coarseness observed in LOM and SEM was also observable for these build orientations. For the 90° orientation the position of the map was unfortunately chosen leading

to a lower quality of the micrograph and pole figure. This also means that the elongated grains and trend in coarseness of microstructure could not be observed in this micrograph.

The pole figures of the α- and γ-phases were used to show that the Burgers (equation 2.2) and Blackburn (equation 2.3) orientation relationships were valid in this material. Sample pole figures can be seen in figure 4.9. It shows that the phases show similar peaks for the relevant planes in the material. This shows that the material did solidify via the path described by equation 2.1.
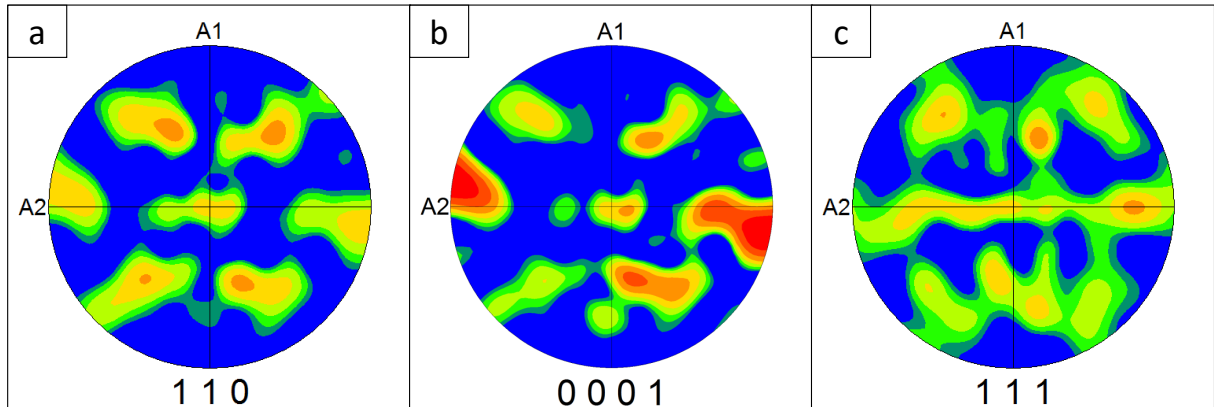
Figure 4.9: Pole figures describing the orientation relationships, exemplary given for the 0° measurement. **a**: β (110) pole figure, **b**: γ (0001) pole figure, **c**: α (111) pole figure.

4.3.5 Phase Analysis

While the EBSD measurements would also allow for a quantitative phase analysis they were discarded, as the clean-up operations shifted the phase fractions. Instead SEM and LOM images were evaluated as well as the XRD patterns gained from measuring the as-EBM material.

In the case of the annealed samples only the XRD-patterns were used for phase analysis as they often exhibited an inhomogeneous microstructure as described in section 4.3.3. This meant, that an analysis of the micrographs would have strongly depended on the position.

While the evaluation of SEM and LOM images resulted in roughly the same phase fractions, the XRD-results differed significantly in the as-EBM material. A likely explanation is the texture already described in section 4.3.4. The Rietveld refinement makes this apparent. In material without any texturization, the calculated patterns should ideally overlap the measured one. The texture results in the presence of preferred lattice orientations, which means that the peaks of some planes are increased in intensity relative to others. This can be seen in figure 4.10. Although methods are available in the evaluation software to correct for this effect, they did not result in a significant improvement. Therefore all the results provided here were calculated without attempting such a correction.

Table 4.4: Quantitative phase analyses were either executed on SEM images or using Rietveld-refinement. The temperatures are refer to the respective heat treatments, the samples were kept at this temperature for 1 h and then an AC step followed.

| sample	method	phase fraction [vol%]		
		α_2	β_o	γ
as EBM 0°	SEM	39	9	52
as EBM 0°	Rietveld	21	10	69
as EBM 45°	SEM	35	14	50
as EBM 45°	Rietveld	23	14	63
as EBM 90°	SEM	35	19	46
as EBM 90°	Rietveld	24	16	60
powder new	Rietveld	77	21	2
powder old	Rietveld	23	7	70
1200 °C	Rietveld	49	8	43
1210 °C	Rietveld	53	6	40
1220 °C	Rietveld	74	6	20
1230 °C	Rietveld	76	3	21
1240 °C	Rietveld	90	4	6
1250 °C	Rietveld	89	8	3
1260 °C	Rietveld	95	2	3
1270 °C	Rietveld	92	5	3
1280 °C	Rietveld	91	3	6
1290 °C	Rietveld	88	3	9
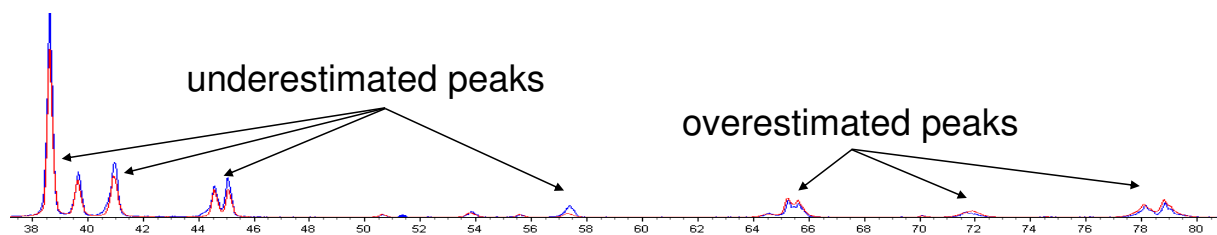
Figure 4.10: The texture present in the EBM samples (in this case at 0° orientation) caused some of the peaks over- and other to be underestimated in terms of their intensity.

4.4 Mechanical Tests

4.4.1 Tensile Tests

The tensile tests were executed for samples of NL+β- and NL+γ-microstructure. A strong difference between the different microstructures and a smaller difference between the differ-

ent build orientations - in particular for the NL+γ-samples - was observed. While the NL+β-microstructure was well adjusted, the NL+γ-samples appeared closer to a triplex microstructure as can be seen in figure 4.11. All NL+β-samples locally exhibited coarser microstructures with a lower amount of β_o-phase (lighter phase). This may be due to the fact that a higher amount of β_o tends to inhibit the coarsening of the material [8]. Likely grains in areas of higher local Al-contens (and therefore lower β_o-fractins) coarsened more strongly than others, leading to this structure. Overall the 0° build orientation sample exhibited a coarser microstructure compared to the other two. This is a result of the flawed heat treatment described in section 3.8.
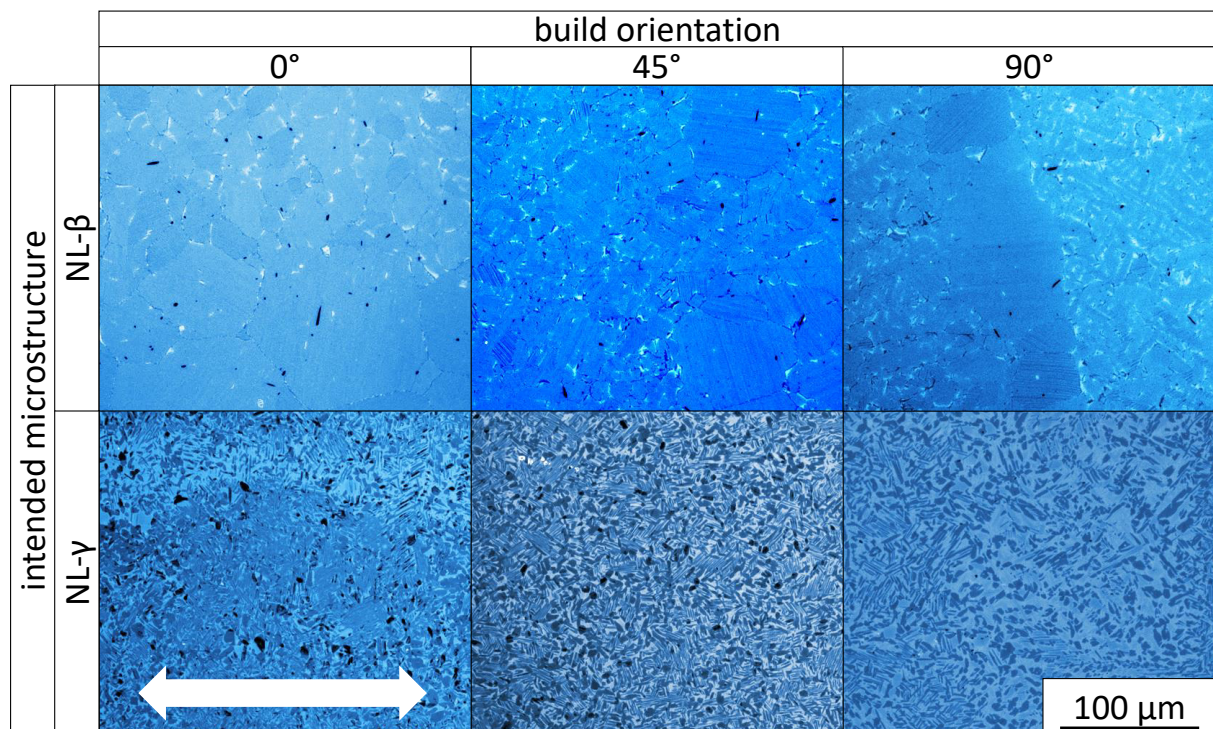
Figure 4.11: LOM images of the microstructure after the tensile tests at 300 °C. The locally coarser grains in the NL+β-samples are visible, they coincide with a lower β_o-phase fraction. In the NL+γ-samples no individual grains are visible.

For all samples after testing either notches were visible in the sample surfaces and/or they broke far from the center of the gauge length. An example of a notch in the surface and of the fracture position along the gauge length can be seen in figure 4.12.

Most samples did not show a high plastic deformation, in some cases not even an $R_{p0.1}$-value could be measured. The specific values for $R_{p0.1}$ and $R_{p0.2}$ (as far as available), R_m as well as the total elongation at fracture are provided in table 4.5.

The stress-strain-curves for the NL+β-microstructure samples are provided in figure 4.13. Only

Table 4.5: The complete list of all the values for $R_{p0.1}$, $R_{p0.1}$, R_m and total elongations at fracture for all the tensile tests executed.

| sample orientation	microstructure	test temperature [°C]	strength [N/mm^2]			elongation at fracture [%]
			$R_{p0.1}$	$R_{pp0.2}$	R_m	
0°	NL+β	300	755	-	776	0.64
45°	NL+β	RT	-	-	829	0.56
45°	NL+β	300	-	-	746	0.53
45°	NL+β	300	799	880	945	0.91
90°	NL+β	RT	-	-	810	0.60
90°	NL+β	300	767	846	849	0.80
90°	NL+β	300	771	853	863	0.82
90°	NL+β	750	493	589	808	1.48
0°	NL+γ	300	-	-	692	0.48
0°	NL+γ	300	-	-	660	0.45
45°	NL+γ	300	-	-	626	0.42
45°	NL+γ	300	777	786	888	1.85
90°	NL+γ	300	678	694	751	1.24
90°	NL+γ	300	658	672	809	2.32

Figure 4.12: Photos of a sample that broke far from the centre of the testing length. The red circle indicates a nick in the surface.

small changes in the stress-strain curves could be observed with regards to the different sample orientations. The 90° build orientation had some plastic deformation for both samples, while for the 45° orientation this occurred only once. The 0° sample exhibited a relatively low plastic deformation. It therefore appears, that the 90° build orientation behaves the most ductile for this microstructure. However, due to the low number of samples this cannot be said with certainty. Similar tensile tests by Todai et al. [44] conducted on a peritectically solidifying γ-TiAl alloy showed a similar trend.

A strong temperature dependence was observed. Although only one sample was tested at RT it appears to have a higher yield strength (although the plastic deformation was so low that not even $R_{p0.1}$ could be measured) than the samples tested at 300 °C. The plastic deformation of the sample at 750 °C exhibited a much larger plastic deformation when compared to the other NL+β-samples. Although no reduction of area was visible after testing and the sample still failed brittle, it behaves more ductile. Brittle-to-ductile transition temperatures (BDTT) around this testing temperature have been reported for γ-TiAl alloys have been reported [11]. For the NL+γ-samples higher elongations to fracture were measured as can be seen in figure 4.14. This is coherent with the fact that $β_o$ is very brittle and generally impedes the material properties at RT. The different orientations showed a stronger change in behaviour when compared to the β-samples, however the trend was the same. The 0° failed without plastic deformation, while the 45° orientation showed considerable plastic strain in one out of two cases while both samples oriented at 90° showed a high elongation at fracture. The triplex microstructure of these samples is expected to behave more ductile [18].

The differences in elongation at fracture of the NL+γ-samples also reflect in SEM micrographs of the fracture mirror. While the 0° orientation showed a significant amount of intercrystalline fracture the 90° orientation showed mostly transcrystalline fracture, often along the γ-lamellae with the 45° orientation being at intermediate levels between the two as can be seen in figure
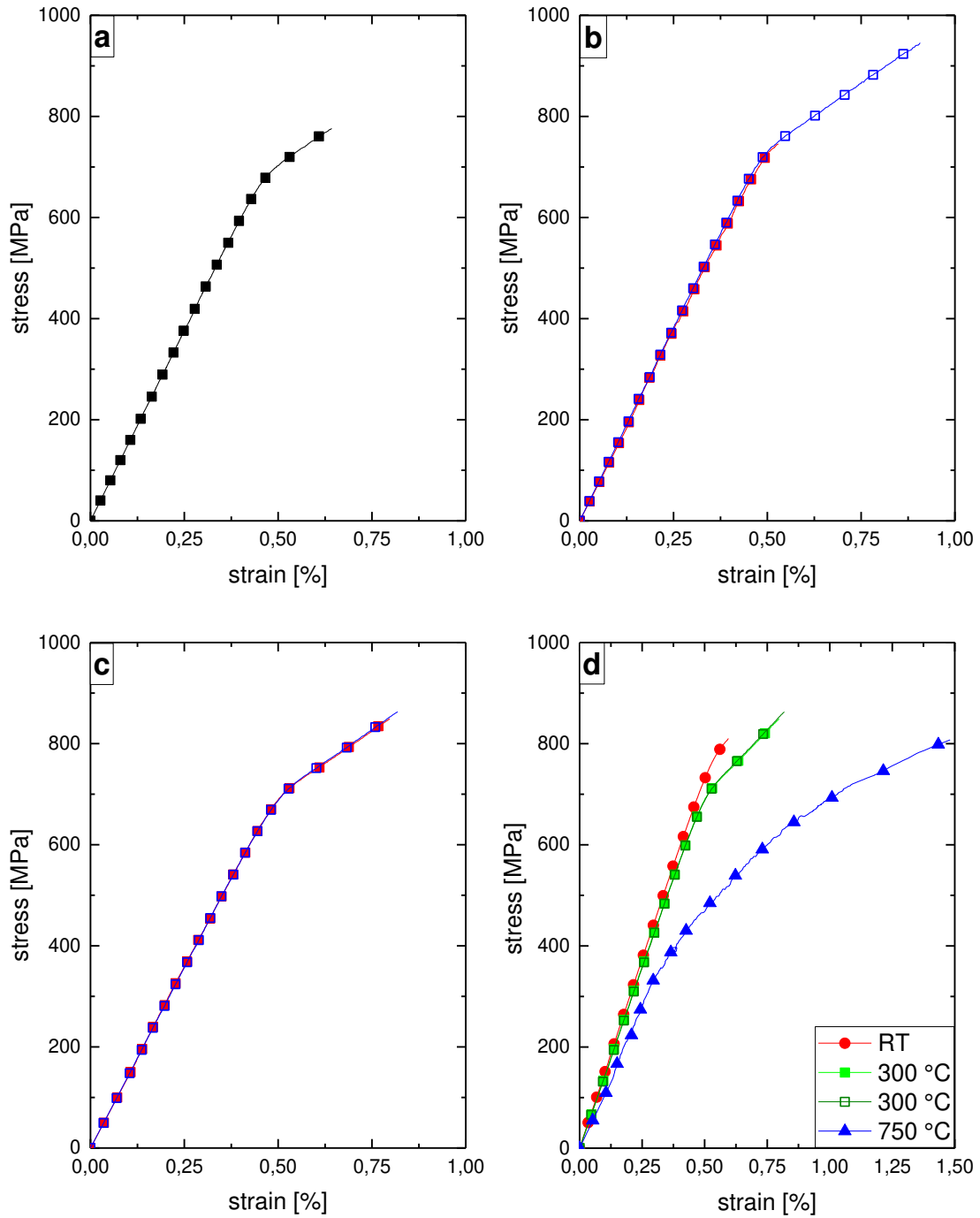
Figure 4.13: Stress-strain curves for the NL+β-samples at 300 °C (unless otherwise specified). **a**: 0° sample orientation - only one sample was measured. **b**: Two 45° samples were measured. **c**: Two 90° samples were measured. **d**: The stress-strain curves varied strongly between samples measured at RT, 300 °C and 750 °C. Note the different scaling of graph **d**.
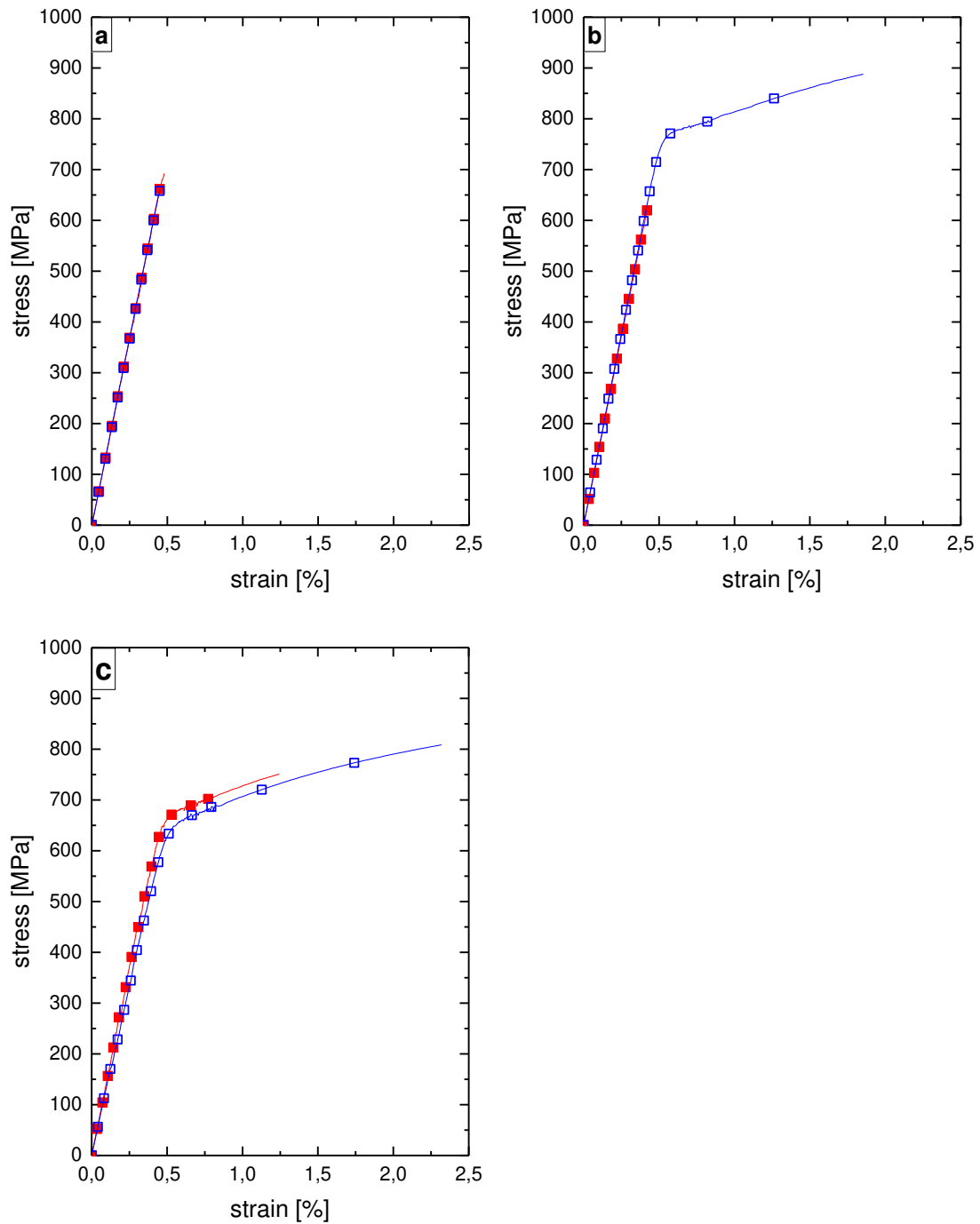
Figure 4.14: Stress-strain curves for the NL+γ-samples at 300 °C. Note the different scaling of the x-axis relative to the curves of the NL+β-samples. **a**: The 0° sample orientation showed almost no plastic strain. **b**: One of two 45° samples showed high plastic strain. **c**: Both of the 90° samples showed high plastic strain.

4.15. This behaviour corresponds to the grain orientation in the material. The highly elongated grains in the material were oriented in such a way, that in the 90° build orientation it was easier to break through the grain than along the boundaries, since a much larger fracture area would be required. For the 0° build orientation this was not the case, therefore a higher amount of intercrystalline fracture occurred. The 45° orientation and therefore the fracture behaviour lies between the other two. In the NL+β-samples on the other hand only transcrystalline break was observed. Often the fracture propagated along the γ-lamellae were found as can be seen in figure 4.16.

In these SEM micrographs often at the starting points structures that appeared "bubbly" were visible. This was very strongly visible in the 90° build orientation sample with NL+β-microstructure (see figure 4.16). Energy dispersive X-ray spectroscopy (EDX) spots of the fracture starting points were made. Ca was found at each of them, a sample pattern can be seen in figure 4.17, how this contamination occurred is unclear. However, it does appear likely that it happened during production of the powder in the atomization process.

An LOM investigation of the fractures was also conducted. To that end the samples were cut along their length axis, embedded in resin and ground and polished until the position visible in the microscope was as close as possible to the position where failure was initiated. As can be seen in figure 4.18 show, in the NL+β-samples large grains could be found close to the fracture. Some cracks going into the material were visible, these often occurred along the γ-lamellae. This is similar to the behaviour observed in the SEM micrographs, where a propagation of the fracture along these lamellae was observable (compare figure 4.16). Differently from the results found by SEM and EDX, in inclusions could be detected. This is likely due to the small size of these inclusions. It therefore seems likely that a combination of inclusions and coarse grains led to material failure in these cases. In NL+γ-samples no coarsening of the grains was visible. This was due to the fact, that the triplex microstructure did not allow do discern between individual grains in the material.
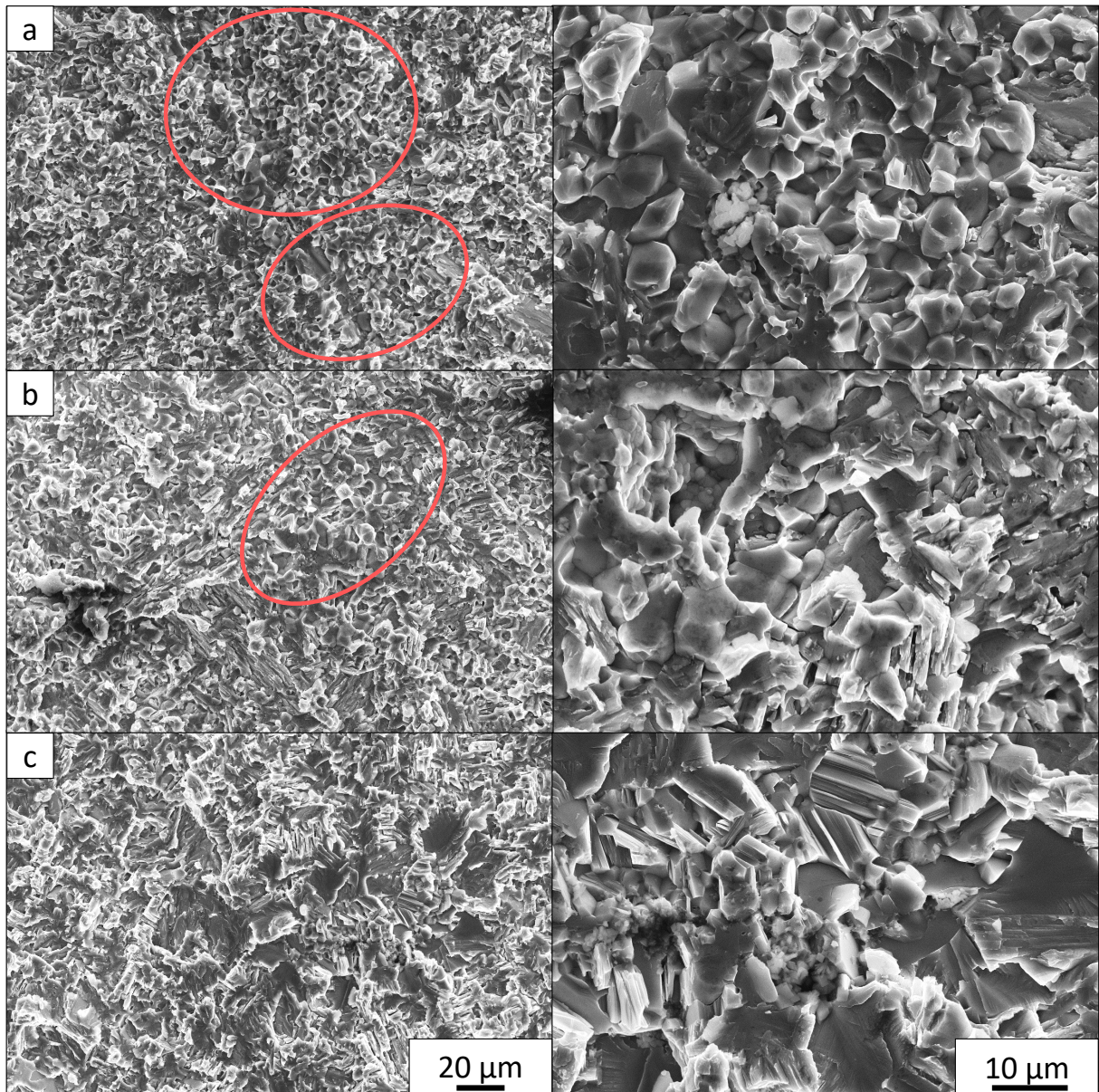
Figure 4.15: Left: SEM micrographs of the fracture mirror of NL+γ-samples with areas showing largely intercrystalline fracture indicated with the red circles. **Right**: SEM images of the (likely) fracture starting points. **a**: The 0° orientation exhibited large intercrystalline areas. **b**: For the 45° less intercrystalline area was found. **c**: The 90° orientation appears to have broken predominantly transcrystalline. The micrographs were made using SE contrast.
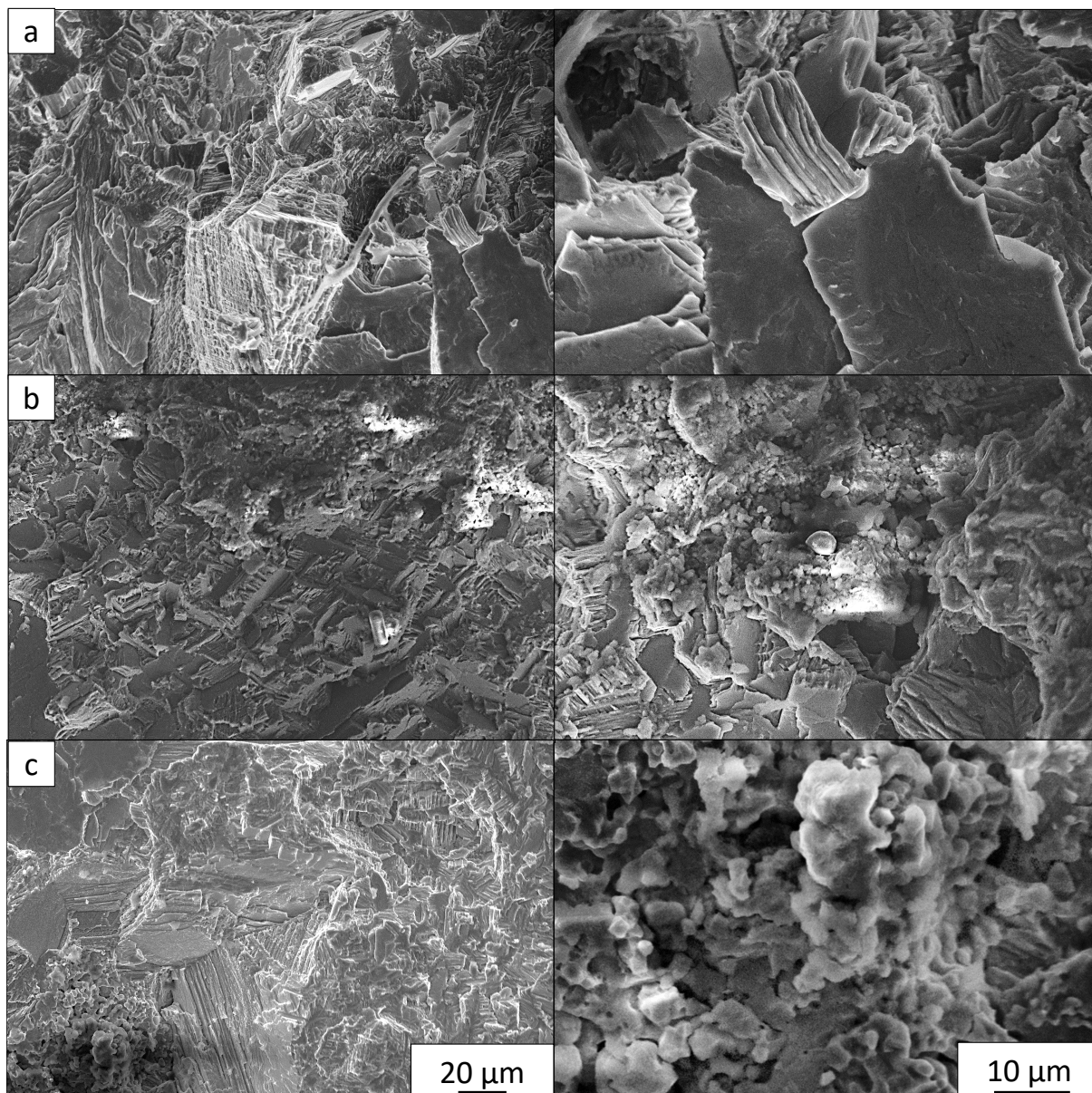
Figure 4.16: Left: SEM micrographs of the fracture mirror of NL+β-samples. The micrographs were made using SE contrast. **Right**: SEM images of the (likely) fracture starting points.
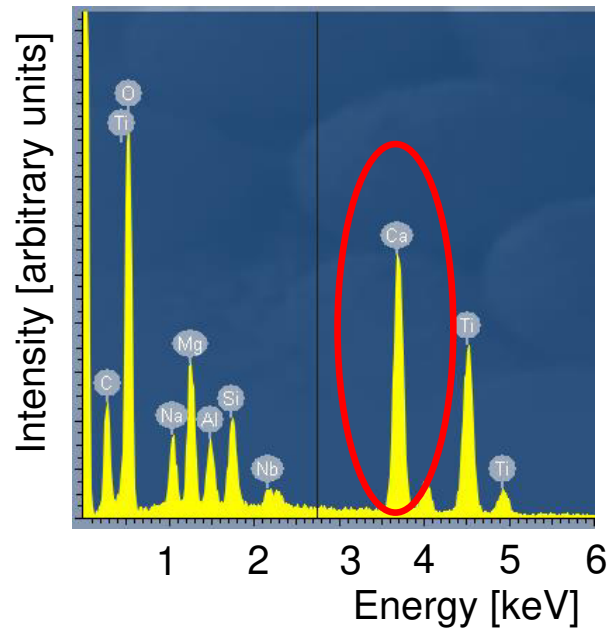
Figure 4.17: The EDX patterns of the fracture starting points showed Ca peaks, indicated by the red circle.
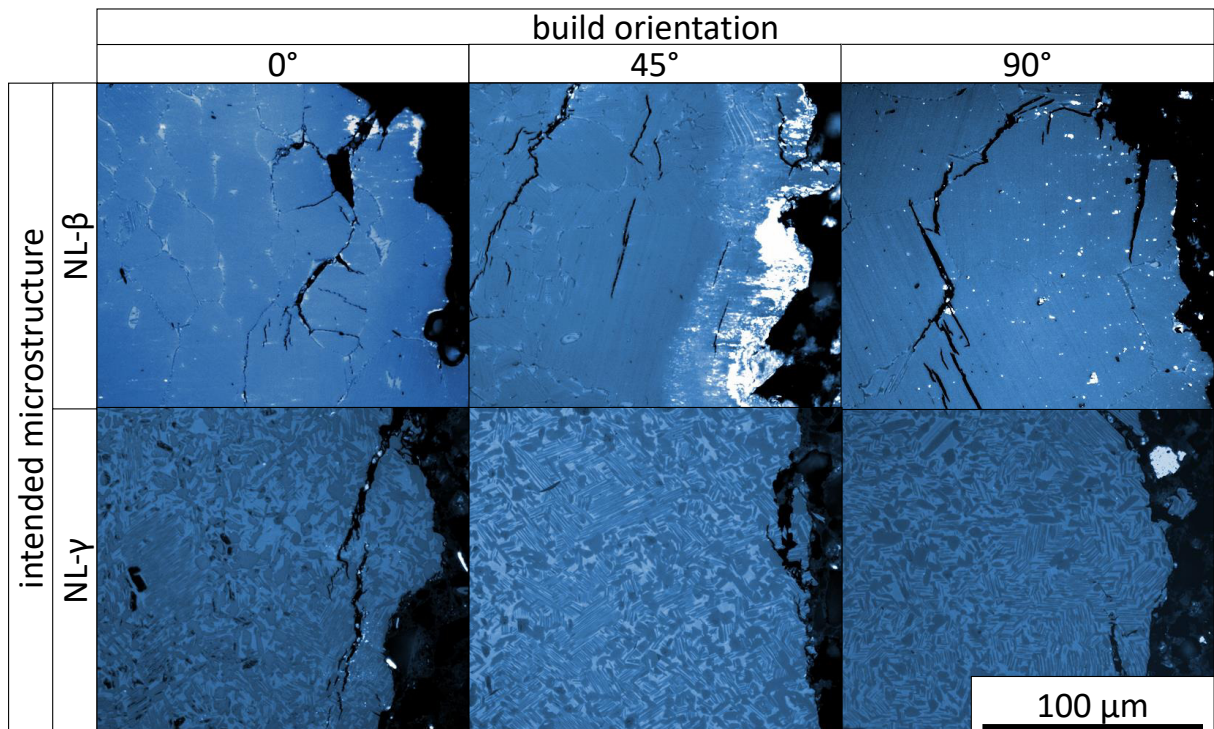
Figure 4.18: LOM images at positions close to the initiation point of fracture. The in the NL+β-samples coarse grains were found close to that position, in the NL+γ-samples no grains were visible.

4.4.2 Creep Tests

The 1000 h creep tests were executed on samples with NL+β-microstructure and showed a strong dependence of the build orientation of the samples on the creep strain rate. The 0° build orientation exhibited the best creep behaviour with the lowest creep strain rate and the lowest creep strain after about 1000 h. The 45° sample showed worse behaviour and 90° the worst. Whether or not this can be purely attributed to the build orientation is doubtful, as the 0° sample was annealed wrongly as described in section 3.8. Due to a lack of samples, no microstructural analysis of the creep samples before testing could be executed. However, the NL+β-samples used for tensile testing at 300 °C provided in figure 4.11 should be similar in that regard. For all measured samples the creep strain after around 1000 h, the minimal creep strain rate and the creep strain at which it occurred are provided in table 4.6 and displayed in figure 4.19. The applied stress and temperature lies in a range that where generally dislocation climb is the dominating creep mechanism for γ-TiAl-alloys [11].

Table 4.6: Strains and strain rates of the three different sample orientations show that the 90° sample has the worst creep resistance of the three samples.

	strain [%]		
sample orientation	after 1000 h	at minimal strain rate	minimal strain rate [$10^{-9}s^{-1}$]
0°	1.14	0.78	2.43
45°	1.63	0.79	3.7
90°	3.03	0.91	7.05

The creep strain rates are comparable to those found by Schwaighofer et al. [45], however in this thesis they differed in terms of their build orientation, while they compared different microstructures. After the creep tests a NL+β-microstructure was observable. The colonies with some $β_o$ and γ remaining along the grain boundaries can be seen in figure 4.20. The size of the $α_2$/γ-colonies varies between some 10 μm for the 45° and 90° orientations and coarser grains in the range of 10 up to well over 100 μm in size for the 0° build orientation. In the 0° build orientation the colony size appears less homogeneous, with areas of much larger colony size being visible between layers of lower size. This can likely be attributed to the wrong heat treatment cycle of this sample as well. Its grains also appear more spherical in shape when compared to the other build orientations. In other, peritectically solidifying, γ-TiAl-alloys fabricated by EBM similar coarser layers have been observed [30, 40, 44, 46].
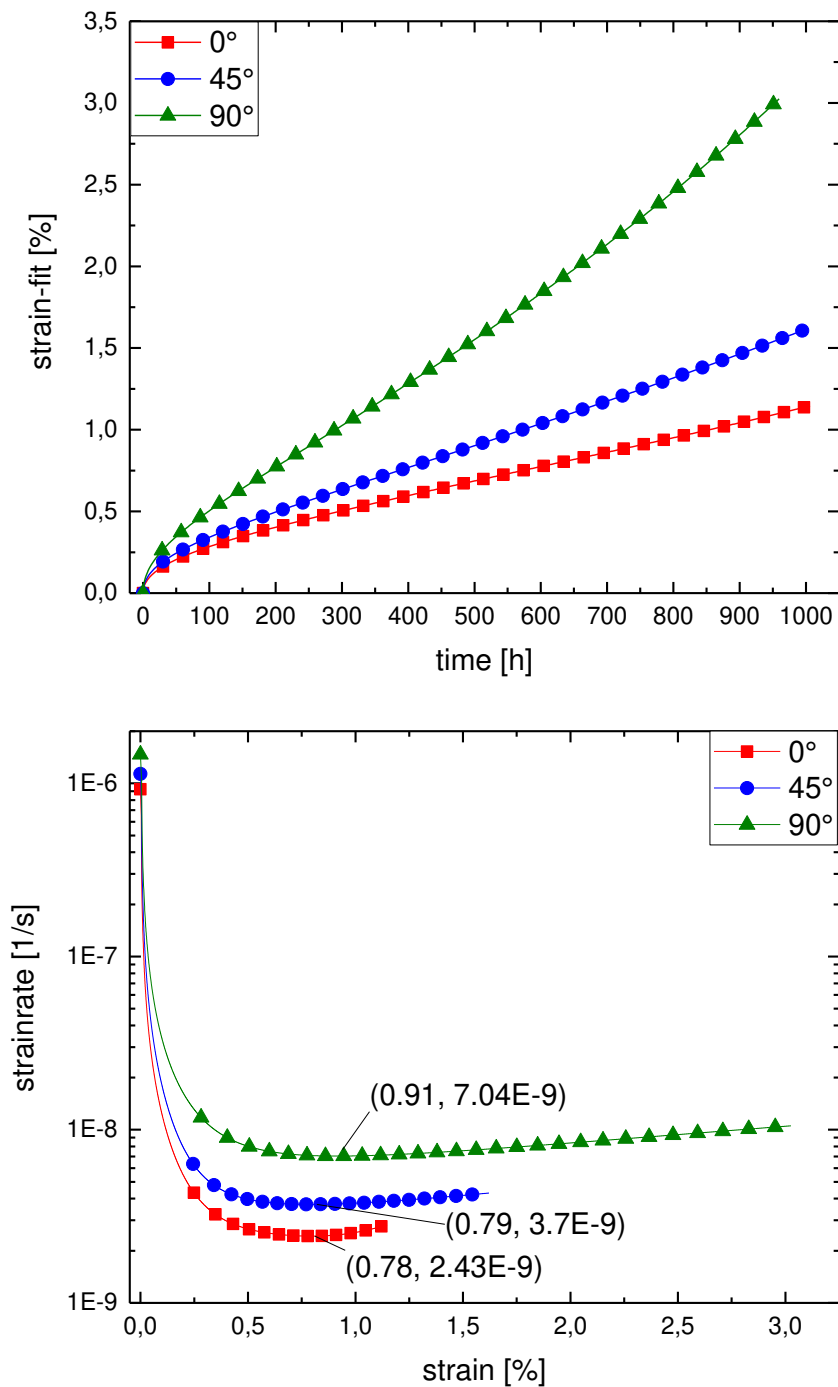
Figure 4.19: Top: Comparison of the different orientations in a time-strain graph. **Bottom**: Strain-strainrate curves for the different orientations. The 90°-sample shows the highest creep strain rate, with 45° being lower and 0° the lowest.
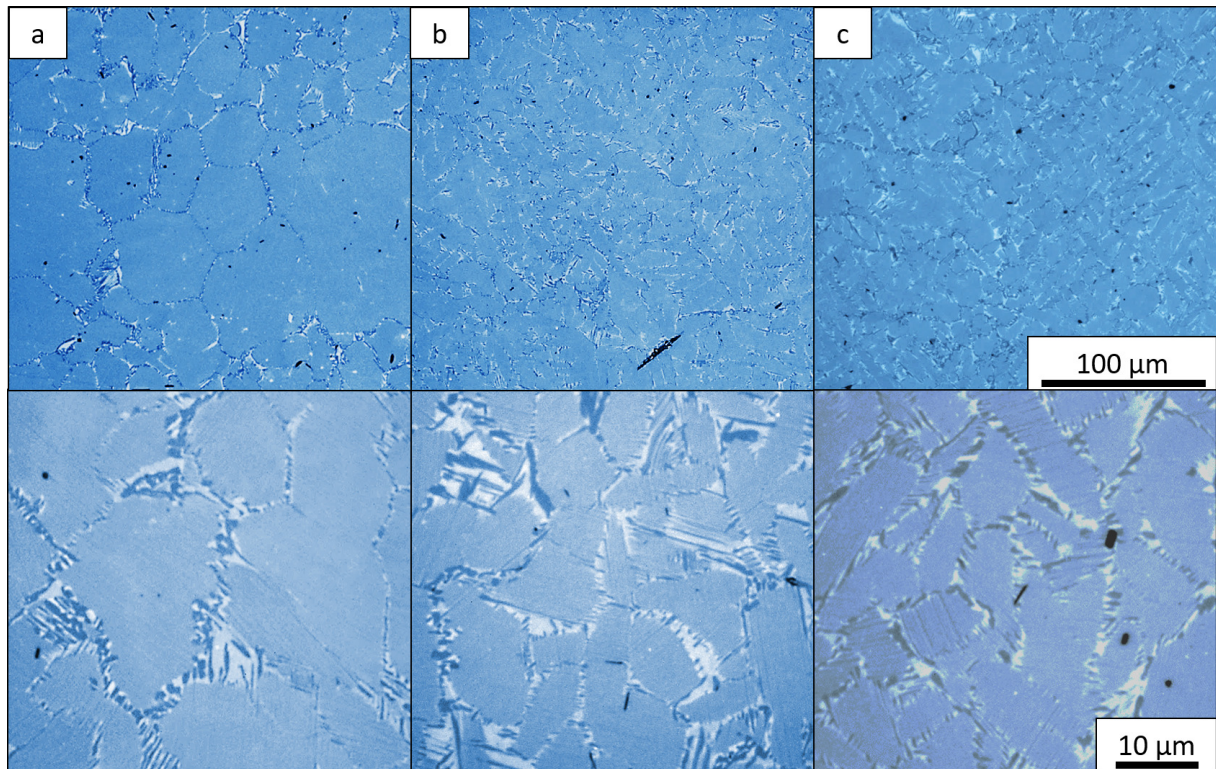
Figure 4.20: LOM images after the creep tests. **a**: 0° orientation, the top image shows the difference in grain size as well as the lower β_o-fraction at the coarser regions. **b**: 45° orientation, the $\alpha_2+\gamma$-colonies are less circular in shape when compared to 0°. **c**: The 90° orientation shows a similar microstructure to 45°.

4.5 Deformation Behaviour

There were significant problems measuring the flow curves in the deformation dilatometer. The ideal sample dimensions for the deformation dilatometer are cylinders of 10 mm in length and 5 mm in diameter, the samples tested were only 8 mm in length and 4 mm in diameter. Therefore the samples tended to get dislodged. In order to avoid this thin Mo-sheets were attached on both faces of the cylinders. Attaching the thermal couples to the centre of the samples often resulted in them getting torn off during the deformation, moving them off center improved this but local temperature changes decreased the accuracy of the measurement. In order to evaluate the temperature shifts along the sample length, two thermal couples were attached, one at the center and one close to one of the faces, about 4 mm apart. The temperatures measured differed up to 20 °C over this distance. The assumption was made that this temperature difference was constant, therefore in order to achieve a temperature of 1200 °C the targeted input into the feedback loop was set to 1220 °C. However, the temperatures measured were only accurate to about 15-20 °C. During the deformation the measured temperature started

to oscillate quite strongly. A sample curve can be seen in figure 4.21. It shows that as the deformation occurred the temperature signal changed. Similar oscillations also occurred in the flow stress (k_f). Therefore the measured data does not accurately depict the behaviour of the material and is only considered in a qualitative manner. A quantitative consideration of $k_{f,max}$ curves is not reasonable because of these measurement errors. The data was therefore only considered in a qualitative manner. After the deformation tests SEM images of the samples
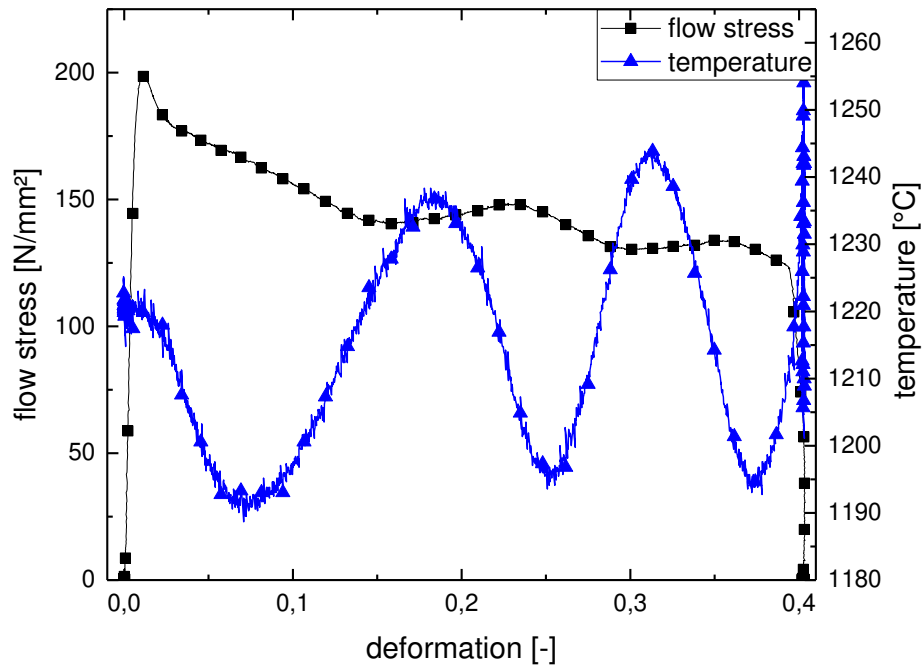
Figure 4.21: Deformation test for a sample of 0° build orientation for a deformation rate of 0.5 s^{-1}. Both the $k_{f,max}$ and the temperature signal exhibited strong oscillations.

cut along their length axis were made in order to investigate the resulting microstructure. Due to the temperature oscillations the different microstructures were not comparable. SEM micrographs of the centres of the deformed samples are provided in figure 4.22. The 0° build orientation deformed at a strain rate of 0.05 s^{-1} showed a large amount of residual γ-phase, among the other samples the 0° orientation at 0.5 s^{-1} and the 90° orientation at 0.5 s^{-1} less residual γ-phase was found. In the samples with 90° orientation at a strain rate of 0.05 s^{-1} and 45° at a strain rate 0.5 s^{-1} no γ-phase was visible. The latter two also showed the strongest recrystallization. As can be seen from these images, no trend as far as microstructure, strain rate, and build orientation was discernible.

The measured $k_{f,max}$ and temperature deviations measured during testing are provided in table 4.7. As can be seen the 45° build orientation had the lowest $k_{f,max}$, 0° the highest. A plau-
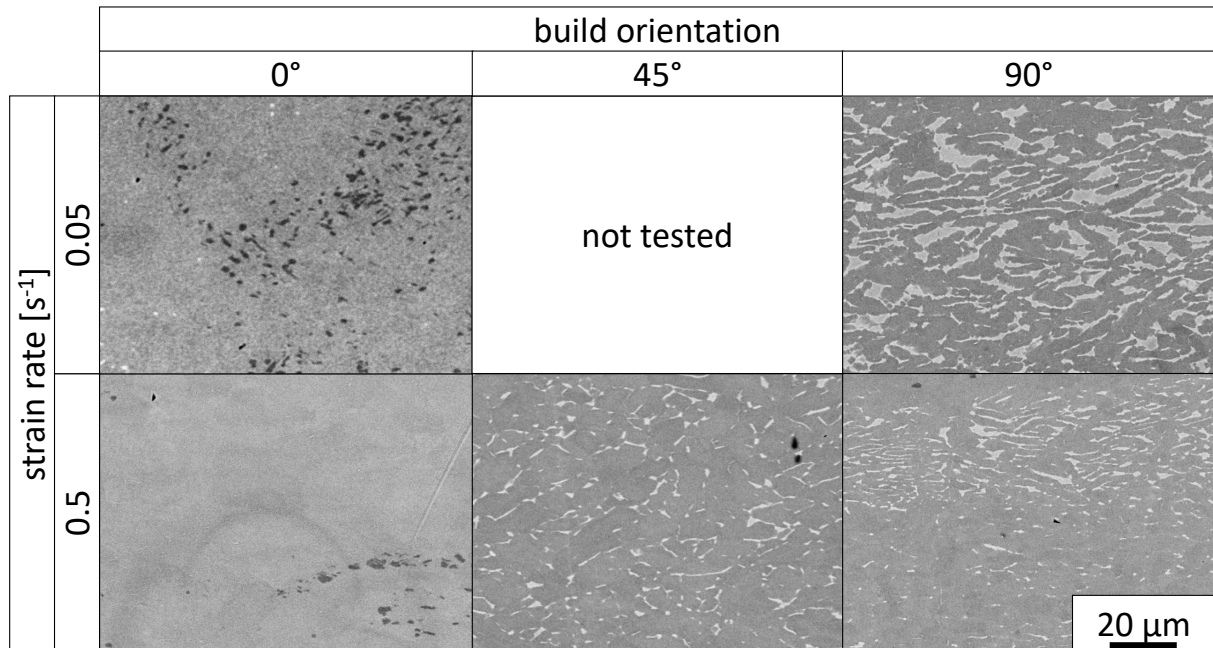
Figure 4.22: SEM micrographs of the different orientations and strain rates did not lead to any conclusive results.

sible explanation for the low $k_{f,max}$ measured in the 45° orientation is gliding along the grain boundaries, which in turn are oriented at 45° relative to the force applied. Although the SEM micrograph revealed that recrystallization occurred, making a evaluation of grain boundary slip difficult, the overall geometry of the sample after the deformation test strongly indicated this behaviour. As can be seen in figure 4.23 the sample faces shifted sideways, which did not occur in the 0° and 90° build orientations. Why the 90° orientation displays an intermediate $k_{f,max}$ is not clear, a possible explanation is the texture in the material that causes many of the slip systems in β and γ to be located at or close to an angle of 45° to the external force, thus maximizing the Schmid-Factor m [47]. However, it is equally possible that the inaccuracies in the temperature control loop caused this behaviour. For a further investigations of the deformation mechanisms other methods, which were not part of this thesis, such as transmission electron microscopy (TEM) would be required. Overall, perhaps a different method such as Gleeble® testing would yield more valuable results when investigating the deformation behaviour of this material. For a more detailed explanation of the slip systems and deformation behaviour of TiAl the reader is referred to the work of Appel et al. [11].

Table 4.7: The maximal $k_{f,max}$ changed with the sample orientation as well as deformation rate $\dot{\varphi}$. Depending on the sample the measured temperature deviated up to $40\,°C$ from the targeted $1200\,°C$.

sample	$\dot{\varphi}$ [s^{-1}]	$k_{f,max}$ [MPa]	temperature deviation [°C]
0°	0.05	92.5	10
0°	0.5	199	40
45°	0.05	-	-
45°	0.5	126	35
90°	0.05	49	15
90°	0.5	158	10
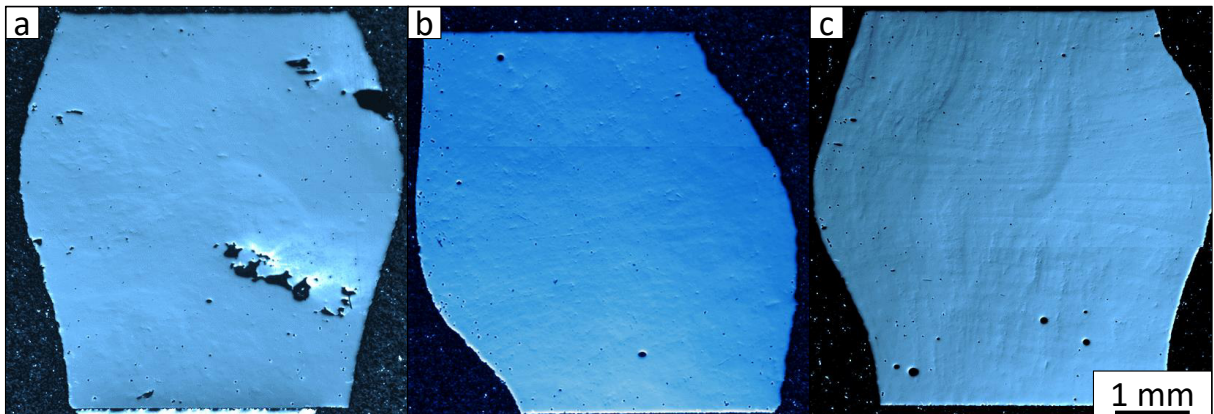
Figure 4.23: a: The sample faces did not shift relative to each other during testing in the 0° build orientation. **b**: The sample faces did shift relative to each other during testing in the 45° build orientation, indicating grain boundary slip. **c**: The sample faces did not shift relative to each other during testing in the 90° build orientation.

5   Summary and Outlook

In the course of this master thesis samples of an intermetallic β-solidifying γ-TiAl alloy called TNM produced by EBM, a powder-bed-fusion AM method, were investigated. The nominal composition of the alloy was Ti with 43.5 at.% Al, 4 at.% Nb and 1 at.% Mo as well as 0.1 at.% B. Analyses of the samples as well as the precursor powder in the as-atomized and recovered states were conducted. The samples produced by EBM were cylindrical in shape and the axes of these cylinders were set to be at angles of 0°, 45° and 90° relative to the base plate. Optical and electron microscopy were used to investigate the differences in microstructure. Heat treatments, thermal analysis and chemical analysis gave insight into the composition of the material. In order to gain information about mechanical and processing properties tensile-, creep- and deformation tests were conducted.

The properties differed strongly dependent on the build orientation of the samples. At 0° build orientation the samples showed the finest microstructure, at 45° the coarsest and at 90° they exhibited intermediate levels. The 0° build orientation samples also were the only ones to show significant amounts of process related bonding errors between material layers. This suggests that the samples oriented at 0° cooled down faster than the others. The reason was found to lie in the scanning strategy, which gave the samples more time to cool down between compared to the other orientations.

EBSD revealed that the solidification conditions in the EBM-process resulted in a $<100>$-texture in the bcc β-phase which also translated into the other faces due to the known orientation relationships in TNM. It may be possible to adjust the alloy composition to avoid this texture, for example peritectically solidifying γ-TiAl alloys do not exhibit such a behaviour [46]. The solidification also resulted in grains of a high aspect ratio growing in the building direction.

The chemical analysis revealed that the powder was not influenced strongly by the EBM process, but in the built material an Al-loss of over 1 at.% could be observed. Other studies have investigated the influence of the energy input in correlation to the changes in chemistry and have found strong correlations. Therefore the adjustment of the process parameters might be part of the solution to this problem. Another approach might be the adaptation of the powder composition to compensate for the Al-loss. This Al-loss did not happen uniformly across the sample, but occurred primarily at the top of the introduced layers. This led to locally different microstructures. Such local changes also influenced the material behaviour during heat treatments, as higher Al-contents allowed for more coarsening of the material to occur.

Two different types of microstructure, NL+β and NL+γ, were chosen to conduct tensile tests. Regardless of microstructure, the 90° build orientation exhibited the most and 0° the least duc-

tile behaviour. In the NL+γ-samples the fracture mirror appeared differently according to the build orientation. At 90° almost the entire area broke transcrystalline. This was due to the grain orientation in the material. The 45° and 0° build orientation samples showed an increasing fraction of intercrystalline area.

Creep tests on samples of a NL+β-microstructure showed the lowest creep strain rate in 0° and the highest in 90° build orientation samples. Whether or not this is an actual result of the build orientation is unclear, as the heat treatment of the 0°-sample was conducted wrongly, further investigations would be required for a more reliable answer.

Deformation testing on as-EBM samples did not yield conclusive results, as the samples did not deform uniformly and problems occurred with the temperature control. Therefore only a qualitative assessment fo the data was possible. It showed, that the 45° build orientation had the lowest $k_{f,max}$. This and the fact that the faces of the sample exhibited a shift relative to each other led to the conclusion that a grain boundary slip was responsible for the low k_f. The 90° samples had higher levels of flow stress, but still lower than 0°. Maybe this was due to the high number of slip systems oriented at about 45° relative to the direction of the applied force in the 90° sample. However, high temperature oscillations during testing impede certain conclusions.

Overall this work revealed, that there are still many problems in when using EBM as a means to fabricate TNM parts. Additional work will be required to gain further insight into the solidification and resulting texture, pile-up and Al-loss. With more knowledge it is likely possible to find process parameters and/or adapt the alloy, making EBM a viable production method for TNM or a similar material. Many other works are currently being conducted, globally as well as at the Montanuniversität Leoben to understand and improve AM of γ-TiAl-alloys.

Possible options for further investigations are additional deformation testing, using different, more suitable methods such as Gleeble®-testing. These would hopefully allow for a more precise temperature control and better reproducibility of the measurements. Additional parameter studies might help to understand the solidification process, resulting microstructure and texture as well as the occurrence of the pile-up in the material. The optimization of the resulting chemical composition and reduction of texture are probably the most important goals that need to be met in order to improve the material for EBM to become a serviceable method of production.

References

[1]   Murr, L. E.; Gaytan, S. M.in Hashmi, Saleem (ed.), "Electron beam melting", Elsevier, Oxford, 2014, p. 135–161.

[2]   C. W. Hull, Apparatus for production of three-dimensional objects by stereolithography, Patent US4575330 A, 1984.

[3]   N. A. B. Nordin, M. A. B. Johar, M. H. I. B. Ibrahim, O. M. F. B. Marwah, Advances in high temperature materials for additive manufacturing, IOP Conference Series: Materials Science and Engineering 226 (2017) 1-8.

[4]   M. Lanaro, D. P. Forrestal, S. Scheurer, D. J. Slinger, S. Liao, S. K. Powell, M. A. Woodruff, 3D printing complex chocolate objects, Journal of Food Engineering 215 (2017) 13–22.

[5]   H. P. Tang, M. Qian, N. Liu, X. Z. Zhang, G. Y. Yang, J. Wang, Effect of powder reuse times on additive manufacturing of Ti-6Al-4V by selective electron beam melting, JOM 67 (2015) 555–563.

[6]   T. Kellner, "An epiphany of disruption: GE additive chief explains how 3D printing will upend manufacturing", https://www.ge.com/reports/epiphany-disruption-ge-additive-chief-explains-3d-printing-will-upend-manufacturing/, 13.11.2017.

[7]   B. Koenig, "3D printing begins to soar in aerospace", http://advancedmanufacturing.org/3ds-test-flight/, 05.01.2018.

[8]   H. Clemens, S. Mayer, Design, processing, microstructure, properties, and applications of advanced intermetallic TiAl Alloys, Advanced Engineering Materials 15 (2013) 191–215.

[9]   S. Mayer, P. Erdely, F. Dieter Fischer, D. Holec, M. Kastenhuber, T. Klein, H. Clemens, Intermetallic β-solidifying γ-TiAl based alloys – from fundamental research to application, Advanced Engineering Materials 19 (2017) 1-27.

[10] J. C. Schuster, M. Palm, Reassessment of the binary aluminum-titanium phase diagram, Journal of Phase Equilibria and Diffusion 27 (2006) 255–277.

[11] Appel, F.; Paul, J. David Heaton; Oehring, M., "Gamma titanium aluminide alloys", Wiley, Weinheim, 2012.

[12] R. Werner, E. Schwaighofer, M. Schloffer, H. Clemens, J. Lindemann, S. Mayer, Constitutive analysis and microstructure evolution of the high-temperature deformation behavior of an advanced intermetallic multi-phase γ-TiAl-based alloy, Advanced Materials Research 922 (2014) 807–812.

[13] H. Clemens, T. Schmoelzer, M. Schloffer, E. Schwaighofer, S. Mayer, G. Dehm, Physical metallurgy and properties of β-solidifying TiAl Based Alloys, MRS Proceedings 1295 (2011) 183.

[14] H. Clemens, Svea Mayer, Intermetallic γ-titanium aluminide based alloys from a metallographic point of view – a continuation, Practical Metallography 48 (2011) 64–100.

[15] F.-S. Sun, C.-X. Cao, M.-G. Yan, S.-E. Kim, Yong-Tailee, Alloying mechanism of beta stabilizers in a TiAl alloy, Metallurgical and Materials Transactions A 32 (2001) 1573–1589.

[16] Z. Mahbooba, H. West, O. Harrysson, A. Wojcieszynski, R. Dehoff, P. Nandwana, T. Horn, Effect of hypoeutectic boron additions on the grain size and mechanical properties of Ti-6Al-4V manufactured with powder bed electron beam additive manufacturing, JOM 69 (2017) 472–478.

[17] A. Nérac-Partaix, A. Menand, Atom probe analysis of oxygen in ternary TiAl alloys, Scripta Materialia 35 (1996) 199–203.

[18] S.-C. Huang, E. L. Hall, Plastic deformation and fracture of binary TiAl-base alloys, Metallurgical Transactions A 22 (1991) 427–439.

[19] M. Galati, L. Iuliano, A literature review of powder-based electron beam melting focusing on numerical simulations, Additive Manufacturing 19 (2018) 1-20.

[20] Arcam, "EBM hardware", http://www.arcam.com/technology/electron-beam-melting/hardware/, 28.02.2018.

[21] Z. C. Cordero, H. M. Meyer, P. Nandwana, R. R. Dehoff, Powder bed charging during electron-beam additive manufacturing, Acta Materialia 124 (2017) 437–445.

[22] C. Körner, Additive manufacturing of metallic components by selective electron beam melting — a review, International Materials Reviews 61 (2016) 361–377.

[23] D. Deng, "Additively manufactured Inconel 718", Linköping University Electronic Press, Linköping, 2018.

[24] X. Gong, T. Anderson, K. Chou, Review on powder-based electron beam additive manufacturing technology, Manufacturing Review 1 (2014) 1-12.

[25] C. Körner, E. Attar, P. Heinl, Mesoscopic simulation of selective beam melting processes, Journal of Materials Processing Technology 211 (6) (2011) 978-987.

[26] T. H. C. Childs, C. Hauser, M. Badrossamay, Selective laser sintering (melting) of stainless and tool steel powders: Experiments and modelling, Proceedings of the Institution of Mechanical Engineers, Part B: Journal of Engineering Manufacture 219 (4) (2006) 339-357.

[27] L. E. Murr, E. Martinez, K. N. Amato, S. M. Gaytan, J. Hernandez, D. A. Ramirez, P. W. Shindo, F. Medina, R. B. Wicker, Fabrication of metal and alloy components by additive manufacturing, Journal of Materials Research and Technology 1 (2012) 42–54.

[28] A. A. Antonysamy, J. Meyer, P. B. Prangnell, Effect of build geometry on the β-grain structure and texture in additive manufacture of Ti6Al4V by selective electron beam melting, Materials Characterization 84 (2013) 153–168.

[29] J. Schwerdtfeger, C. Körner, Selective electron beam melting of Ti–48Al–2Nb–2Cr, Intermetallics 49 (2014) 29–35.

[30] H. P. Tang, G. Y. Yang, W. P. Jia, W. W. He, S. L. Lu, M. Qian, Additive manufacturing of a high niobium-containing titanium aluminide alloy by selective electron beam melting, Materials Science and Engineering: A 636 (2015) 103–107.

[31] W. Schatt, K.-P. Wieters, B. Kieback, "Pulvermetallurgie", Springer-Verlag, s.l., 2007.

[32] B. Böck, "Untersuchung und Verifizierung des quasibinären Zustandsdiagramms für beta-erstarrende TNM-Legierungen auf Basis von Ti-(41-45)Al-4Nb-1Mo-0.1B", Montanuniversität Leoben, 2008.

[33] Menczel, J. D.; Judovits, L.; Prime, R. Bruce; Bair, H. E.; Reading, M.; Swier, S., "Thermal analysis of polymers: fundamentals and applications", John Wiley Sons, Inc, Hoboken, NJ, USA, 2009.

[34] L. Spieß, G. Teichert, R. Schwarzer, H. Behnken, C. Genzel, "Moderne Röntgenbeugung", Vieweg+Teubner Verlag / GWV Fachverlage GmbH Wiesbaden, Wiesbaden, 2009.

[35] E. Ence, H. Margolin, Phases in titanium alloys identified by cumulative etching, JOM 6 (1954) 346–348.

[36] F. Garofalo, "Fundamentals of creep and creep-rupture in metals", The Macmillan Co, London, 1965.

[37] A. J. McAlister, D. J. Kahan, The Al–Pt (aluminum-platinum) system, Bulletin of Alloy Phase Diagrams 7 (1986) 47–51.

[38] M. Kastenhuber, T. Klein, B. Rashkova, I. Weißensteiner, H. Clemens, S. Mayer, Phase trans-
      formations in a β-solidifying γ-TiAl based alloy during rapid solidification, Intermetallics 91
      (2017) 100–109.

[39] Telephone Conference with Franke, M. (Neue Materialien Fürth), 27.09.2017.

[40] S. Biamino, A. Penna, U. Ackelid, S. Sabbadini, O. Tassa, P. Fino, M. Pavese, P. Gen-
      naro, C. Badini, Electron beam melting of Ti–48Al–2Cr–2Nb alloy, Intermetallics 19 (2011)
      776–781.

[41] S. M. Gaytan, L. E. Murr, F. Medina, E. Martinez, M. I. Lopez, R. B. Wicker, Advanced metal
      powder based manufacturing of complex components by electron beam melting, Mate-
      rials Technology 24 (2013) 180–190.

[42] A. Kirchner, B. Klöden, J. Luft, T. Weißgärber, B. Kieback, Process window for electron beam
      melting of Ti-6Al-4V, Powder Metallurgy 58 (2015) 246–249.

[43] J. Raplee, A. Plotkowski, M. M. Kirka, R. Dinwiddie, A. Okello, R. R. Dehoff, S. S. Babu, Ther-
      mographic microstructure monitoring in electron beam additive manufacturing, Scientific
      reports 7 (2017) 1-16.

[44] M. Todai, T. Nakano, T. Liu, H. Y. Yasuda, K. Hagihara, K. Cho, M. Ueda, M. Takeyama, Effect
      of building direction on the microstructure and tensile properties of Ti-48Al-2Cr-2Nb al-
      loy additively manufactured by electron beam melting, Additive Manufacturing 13 (2017)
      61–70.

[45] E. Schwaighofer, H. Clemens, S. Mayer, J. Lindemann, J. Klose, W. Smarsly, V. Güther, Mi-
      crostructural design and mechanical properties of a cast and heat-treated intermetallic
      multi-phase γ-TiAl based alloy, Intermetallics 44 (2014) 128–140.

[46] M. Seifi, A. A. Salem, D. P. Satko, U. Ackelid, S. Lee Semiatin, J. J. Lewandowski, Effects
      of HIP on microstructural heterogeneity, defect distribution and mechanical properties
      of additively manufactured EBM Ti-48Al-2Cr-2Nb, Journal of Alloys and Compounds 729
      (2017) 1118–1135.

[47] G. Gottstein, "Physical foundations of materials science", Springer Berlin Heidelberg,
      Berlin, Heidelberg, 2004.